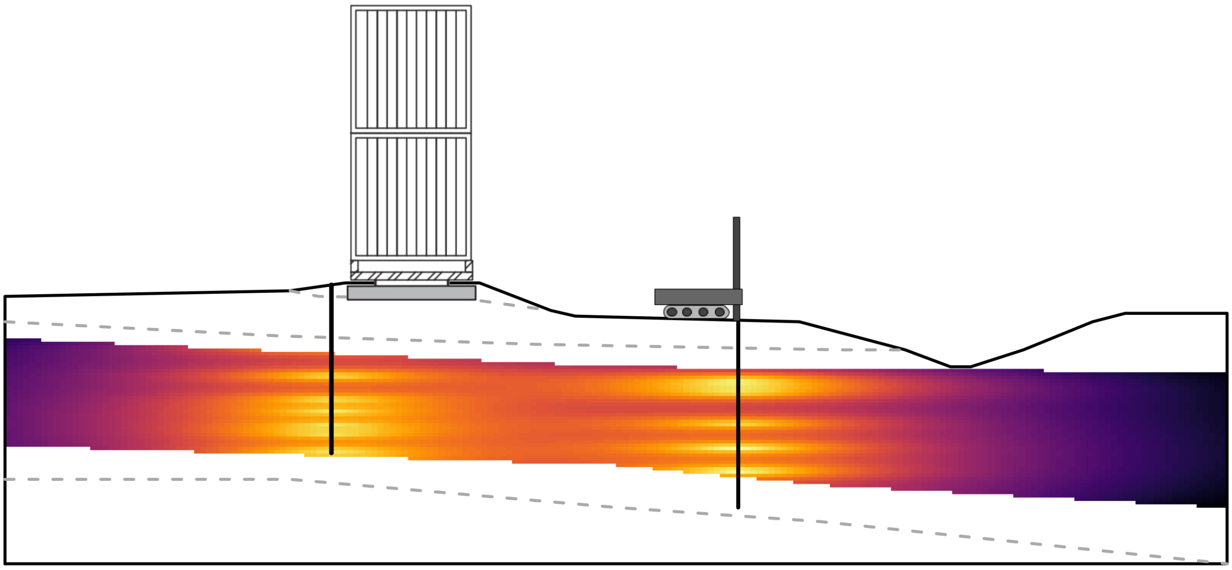

Modelling Spatial Uncertainty in Geotechnics: Benchmarking on Perniö Test Embankment

Master of Science Thesis in the Masters Programme Infrastructure and Environmental Engineering

TOMMY PAP

Master's thesis BOMX02-17-67
Department of Architecture and Civil Engineering
Division of Geology and Geotechnics
CHALMERS UNIVERSITY OF TECHNOLOGY
Gothenburg, Sweden 2017

Master's thesis

Modelling Spatial Uncertainty in Geotechnics: Benchmarking on Perniö Test Embankment

TOMMY PAP

Department of Architecture and Civil Engineering
Division of Geology and Geotechnics
Chalmers University of Technology
Gothenburg, Sweden 2017

Modelling Spatial Uncertainty in Geotechnics: Benchmarking on Perniö Test Embankment
TOMMY PAP

Supervisor: Associate Professor Jelke Dijkstra, Department of Architecture and Civil Engineering, Division of Geology and Geotechnics

Examiner: Professor Minna Karstunen, Department of Architecture and Civil Engineering, Division of Geology and Geotechnics

Master's Thesis BOMX02-17-67
Department of Architecture and Civil Engineering
Division of Geology and Geotechnics
Chalmers University of Technology
SE-412 96 Gothenburg
Telephone +46 31 772 1000

Cover: Perniö test embankment with a random field of sample anisotropic kriging variance

Typeset in LaTeX
Printed by Chalmers Reproservice
Gothenburg, Sweden 2017

Modelling Spatial Uncertainty in Geotechnics: Benchmarking on Perniö Test Embankment
Master of Science Thesis in the Masters Programme Infrastructure and Environmental Engineering
TOMMY PAP
Department of Architecture and Civil Engineering
Division of Geology and Geotechnics
Chalmers University of Technology

Abstract

Natural geomaterials are anisotropic and will always have a degree of uncertainty due to the geological and loading history. In today's engineering practice, however, design calculations are restricted by one deterministic analysis. This leads to characteristic values to be picked on the 'safe side' and thus to overly conservative, hence costly, designs with an unknown degree of uncertainty. An alternative method to approach the problem, as adopted in this Thesis, is to use a probabilistic method that includes the spatial variability in soil properties in the analysis. In this case the Random Finite Element Method is used for the first time with a realistic constitutive model for the soil. As a result rather than varying an arbitrary undrained shear strength property the pre-consolidation pressure is varied. This, for the first time, leads to a RFEM method where stiffness and strength, which are stress path dependent, emerge from the spatial variation in pre-consolidation pressure. Furthermore the appraoch is benchmarked against a well documented test site where an old railway embankment on soft soil which was brought to failure. The spatial variation is estimated by transformed Gaussian fields using kriging interpolation and analyzed by 500 Monte Carlo simulations within a Finite Element framework. The results show that spatial variation of apparent preconsolidation pressure influence the embankment stability with up to 10 %. The research also highlights the uncertainties due to sample locations and its influence on the results.

Jord är ett anisotropiskt material med spatial variation. Enligt nuvarande geoteknisk dimensionerings praxis, representeras jordmaterialparametrar av karaktäristiska värden och beräknas med en enda deterministisk analys. Detta leder till val av karaktäristiska värden på den "säkra sidan" och således till dyra och konservativa dimensioneringar med en ouppskattbar andel osäkerhet. En av anledningarna till denna förenkling är beräkningskapacitet, men på senare år har denna ökat avseendevärt vilket möjliggör för metodik med flera simuleringar, så kallad probabilistisk analys, där parameter osäkerhet kan uppskattas. I detta examensarbete evalueras en probabilistisk modell av Perniö skredexperimentet, en järnvägsbank på lera lastat till brott, mot fältmätningar. Studien påvisar osäkerheterna i brottslast, brottstyp samt deformationer, orsakat av den spatial variation av förkonsolideringstryck. Variationen är uppskattad med transformerade Gaussiska fält från kriging interpolation och beräkningarna utförda genom 500 Monte Carlo simuleringar av Finita Elementmetoden. Resultatet visar att den spatial variation av förkonsolideringstryck påverkar järnvägsbankens stabilitet med upp till 10%*. Forskningen belyser även osäkerheter orsakat av provtagningens placering utifrån resultatet.*

Keywords: Embankment stability, Reliability, Kriging interpolation, Monte-Carlo simulations, Probabilistic model, RFEM, Soft clay, Python.

Acknowledgements

This thesis would not have been possible without the guidance, support and encouragement of my advisor, Ass. Prof. Jelke Dijkstra, and Prof. Minna Karstunen, at Chalmers University of Technology, their experience in advanced numerical modelling and understanding of soft soil behavior have been invaluable. My gratitude's extends further to among others:

Dr. Ville Lehtonen at Tampere University of Technology for his enthusiasm and willingness to provide both data and details regarding Perniö study site.

Prof. Gregor Laaha at the Institute of Applied Statistics and Computing (IASC) in Vienna, who was the first to introduced me to statistics and inspired me to learn more about statistical programming.

Division leader Bernhard Gervide Eckel and Dr. Jimmy He at Norconsult AB in Gothenburg, for their interest and support of my thesis.

My beloved family; for their devoted support, understanding and willingness in listening to my complaints; and friends, for treating me with well needed beers in those vitamin D deficient times.

Finally, I would also like to gratefully acknowledge members of the R-bloggers and Stack Overflow communities for their assistance during some of those all-night coding sessions.

Tommy Pap , Gothenburg, July 5, 2017

Tommy Pap

Contents

List of Figures . . . xi
List of Tables . . . xiii
List of Notations . . . xv

1 Introduction 1
1.1 Introduction . . . 1
1.2 Background . . . 1
1.3 Aims & objectives . . . 2
1.4 Thesis outline . . . 2

2 Theory 3
2.1 Reliability Based Design . . . 3
2.1.1 Sources of Uncertainty in Geotechnics . . . 3
2.1.2 Earlier Research . . . 4
2.1.3 Probabilistic Models . . . 5
2.2 Probability . . . 6
2.2.1 Discrete Random Variables . . . 6
2.2.2 Continuous Random Variables . . . 6
2.2.3 Moments of a Distribution: Mean and Variance . . . 7
2.2.4 Covariance and Correlation . . . 8
2.2.5 Linear Regression Model . . . 9
2.2.6 Spatial Interpolation . . . 10
2.3 Geostatistics . . . 11

3 Methods 14
3.1 Outline . . . 14
3.2 Study Site . . . 15
3.2.1 Perniö Test Embankment . . . 15
3.2.2 Site Conditions . . . 16
3.2.3 Constitutive Soil Models and Parameters . . . 16
3.2.4 Spatial Variation of OCR . . . 18
3.3 Kriging Interpolation . . . 19
3.3.1 Homogeneous Random Field . . . 21
3.3.2 Anisotropic Random Field . . . 22
3.4 Spatial Estimation of OCR Used for Analysis . . . 23
3.4.1 Deterministic analysis . . . 23
3.4.2 Probabilistic analysis . . . 24
3.5 Numerical model . . . 24
3.5.1 Estimation of Failure load, deformations and failure mechanism . . . 26

4 Results 27
4.1 Horizontal displacements . . . 28
4.2 Embankment Failure load . . . 29
4.3 Failure mechanism . . . 30
4.4 The spatial effect of apparent preconsolidation pressure on failure load . . . 31

5 Conclusions & Recommendations 33

References 35

Appendix A Perniö test site location **I**
A.1 Data availability I
A.2 Location maps I
A.3 Elevation map, scale 1:8000 II
A.4 Aerial map, scale 1:8000 III
A.5 Soil map, scale 1:8000 IV

Appendix B Perniö Test data **V**
B.1 Site investigation Perniö V
B.2 Instrument locations Perniö VI

Appendix C **VII**

List of Figures

2.1 The reliability of measurements or evaluated results to a reference value is measured in precision and accuracy, figure created by Pekaje (2017) 3
2.2 Sources of uncertainties in risk analysis after (Baecher and Christian, 2003). 4
2.3 Comparison between: one deterministic analysis and two probabilistic analysis with and without spatial variation taken in account 5
2.4 A random variable $X(\omega)$ with three random samples. 6
2.5 Probability Density Function (left) and Cumulative distribution function (right) of a normal distribution. 7
2.6 Figure of two random variables X and Y and their bivariate probability density function $\mathrm{f}_{xy}(x, y)$ 9
2.7 An example of fitting a simple linear regression model to measured data: a) observed data points , b) Fitted linear model with $min(RSS)$ residual distance in black and c) shows the final model with a 95% confidence interval boundries. 10
2.8 Illustration of 2D interpolation; where a) shows the unsampled point Z^* being estimated by both local b) and global c) interpolation; where Z_α is the measured data point and d_α its distance from Z^*. 11
2.9 Definitions of the correlation parameters in the variogram 12
2.10 Two signals: with and without spatial correlation 12
2.11 Two variograms to corresponding signal: showing spatial correlation and a random structure 13
2.12 The influence of different degrees of anisotropy on the Gaussian random field 13
3.1 Figure of the method procedure in four stages 14
3.2 Perniö test embankment with the placement of loading carts and measuring instrumentation before the test procedure (Lehtonen et al., 2015) 15
3.3 The cross-section of study at Perniö test embankment, together with subsoil layers and the position of borehole 43 and 44. 16
3.4 The spatial variation of OCR in borehole 43 and 44 on site and the estimation of OCR as the ratio of in-situ effective vertical stress, σ'_v, preconsolidaion pressure, σ_p. 18
3.5 Normallity check of OCR Data through a QQ-plot and omnidirectional variogram of OCR data showing the exponential model fit. 19
3.6 Figure of two homogenous random fields $\xi = 1$: illustrating the OCR estimation (top) and variance (bottom) over the domain of study 21
3.7 Figure of two anisotropic random fields, where $\xi = 10$: illustrating the OCR estimation (top) and variance (bottom) over the domain of study 22
3.8 The down-scaled anisotropic random fields 23
3.9 OCR datasets used for the determinsistic analysis 23
3.10 A RFEM field of size 60 × 12 masked to the clay layer of study 24
3.11 Geometry and bound conditions of the numerical model with inclinometers used for benchmarking 25
3.12 Measure loading procedure and model phases for Perniö test embankment . 26
4.1 Horizontal displacements and failure mechanism for the Perniö test embankment from the deterministic analysis of E_{OCR} 27
4.2 Benchmarking of horizontal displacements from deterministic and probabilistic analyses in inclinometer observations 28

4.3 Benchmarking of Perniö embankment failure load: Probabilistic approach compared to the deterministic analyses and observed value. 29
4.4 Benchmarking of Perniö embankment failure load: Probabilistic approach compared to the deterministic analyses and observed value. 30
4.5 Comparing simulated RFEM failure modes to field observations presented in Lehtonen et al. (2015). 31
4.6 The resulting OCR variation for: (a), the largest failure load F_{max}; (b), the smallest failure load F_{min} ; and (c), the OCR difference between (a) and (b). 32
A.1 Geographical location of Perniö testing site. I

List of Tables

3.1 Material model parameters set for subsoil layers 17
3.2 Summary of Perniö variogram parameters 20
3.3 PLAXIS phases 26
4.1 Summary of deterministic results in Perniö embankment failure load 29
C.1 Summary of borehole data used for the study at the Perniö test embankment. VII

List of Notations

Following lists describes abbreviations and symbols used in the thesis

Abbreviations

CDF	Cumulative Distribution Function
CoV	Coefficient of Variation
FEM	Finite Element Method
FORM	First Order Reliability Method
FOS	Factor of Safety
FOSM	First Order Second Method
IDW	Inverse Distance Weighting
LEM	Limit Equilibrium Method
MC	Monte Carlo
OCR	Overconsolidation Ratio
PDF	Probability Distribution Function
PMF	Probability Mass Function
QQ	Quantile-Quantile
RBD	Reliability Based Design
RF	Random Function
RFEM	Random Finite Element Method
RSS	Residuals Sum of Squares
RV	Random Variable
SORM	Second Order Reliability Method
ULS	Ultimate Limit State

Terminology descriptions

Descriptions of frequent used terminology:

Deterministic model refers to a tool for estimating the a potential outcome in which no randomness is involved. A deterministic model will thus always produce the same output from a given starting condition or initial state.

Probabilistic model or *stochastic model*, refers to a tool for estimating probability distributions of potential outcomes by allowing for random variation in one or more inputs over time. The random variation is usually based on fluctuations observed in data.

Reliability the degree to which the result of a measurement, calculation, or specification can be depended on to be accurate.

Aleatoric uncertainty or *Natural variability*, refers to the randomness of natural processes created by its temporal and spatial variability.

Epistemic uncertainty or *Knowledge uncertainty*, refers to the uncertainty due to lack of knowledge or understanding of the site.

Bias The amount of inaccuracy in a measurement or calcualtion

Variability The amount of imprecision in a measurement or calcualtion

1 Introduction

1.1 Introduction

Natural geomaterials are anisotropic and will always have a degree of uncertainty due to the geological and loading history. As a result it is explicitly stated in the current geotechnical Eurocode EN 1997-1:2004 (2004) that this variation has to be accounted for. In today's engineering practice, however, design calculations are restricted by one deterministic analysis. This leads to characteristic values to be picked on the 'safe side' and thus to overly conservative, hence costly, designs with an unknown degree of uncertainty. Hence, an increasing research community argues that geotechnical design methods should adapt such that uncertainties due to soil variations is properly incorporated (Phoon and Retief, 2016; Hicks and Jommi, 2014; Bakhtiari, 2011; Griffiths and Fenton, 2007; Baecher and Christian, 2003; Peschl and Schweiger, 2003; Alén, 1998; Larsson et al., 2005; Vanmarcke, 1977). One of those alternative approaches is to use a probabilistic model, which estimates the uncertainty through the probability of failure. Through this approach, the variation of parameters can be modelled and uncertainties assessed in a more quantitative manner then compared to the deterministic models used today.

The Random Finite Element Method (RFEM), is a probabilistic model which takes spatial variation in account by an certain parameter using random field theory (Fenton and Griffiths, 2008). It is one of many available probabilistic methods, but the use of these in practice have so far been sparse. In a special issue on this topic in the journal *Géotechnique*, Hicks (2005) argues that it may be due to a understandable reluctance to change long-established working methods, as well as for the demanding computational effort required in addition none of these methods have been properly validated for a field case. Nonetheless, in recent years scientific progress and computer speed has increased substantially. This enables the necessary step towards a more reliability-based philosophy.

1.2 Background

In Scandinavia, a considerable amount of infrastructure is constructed on embankments on soft soils. Stability assessment of these embankments are usually preformed with traditional limit equilibrium methods. But these methods give inaccurate results, since they do not account for; sequential loading, structural elements, non-elliptic failure surfaces and the complex stress-strain behaviour in soft soils Matthews et al. (2014). Hence, it is shown that the Finite Element Method (FEM) gives a more accurate result in more complex cases. But the precision due to spatial or temporal parameter variation and soil model uncertainty still is not accounted for. As a result improved Ultimate Limit State (ULS) methods for embankment stability are still needed.

In Finland, a full-scale embankment failure test was conducted in 2009 (Lehtonen et al., 2015). The test site, from now on referred to as the *Perniö test embankment*, aimed to provide more data for research on improving calculation methods on embankment stability. In an existing study by Mansikkamäki (2015) the performance of different soil models incorporated in FEM were benchmarked using analysis of the Perniö embankment. The results showed that advanced anisotropic soft soil models, such as S-CLAY1S, showed overall better accuracy in estimating pre-failure behavior, such as deformations and pore pressures. But did not outperform any of the simpler models in terms of the ULS failure load. This indicates that the effect of parameter uncertainty do to natural variation could still be a significant contributor to the uncertainty in ULS analysis.

1.3 Aims & objectives

The aim is to study the uncertainties of: embankment failure load, pre-failure displacements and failure mode due to the spatial variation of the apparent preconsolidation pressure is studied. Both Deterministic and probabilistic models are benchmarked against a well documented field case with ample data on the soil properties and the monitored mechanisms in during the failure test. This leads to the following objectives:

- Use of the Random Finite Element Method (RFEM) with a realistic non-linear soil model for soft soils where the strength emerges as function of stress path
- Benchmark the RFEM against a well documented field case on embankment failure
- Develop the necessary numerical tools for probabilistic interpretation of laboratory data
- Create a probabilistic front end for a commercially available deterministic FE software package (PLAXIS).

1.4 Thesis outline

Including this introduction, the thesis includes five chapters, three appendices and a reference list.

Theory Gives a necessary theoretical review regarding: uncertainties, previous research and probabilistic methods in geotechnics and random field theory.

Methods Proposes the methodology of the study and assumptions for the random field generation of the deterministic and probabilistic datasets used in the analysis. Finally, the numerical model is described with all corresponding parts used to compute failure load, failure mechanism and pre-failure deformations.

Results Presents the study finding from both the deterministic and probabilistic model. All results are compare to field observations from the failure test.

Conclusions Reviews the main findings and gives some recommendations for future research.

Appedices, I-III Provides additions information regarding the Perniö test site.

2 Theory

This chapter aims to introduce readers unfamiliar to the probabilistic methodology used in this thesis. If confident, it is possible to skip this chapter and come back later if necessary. The chapter consists of following three sections:

Section 1: Reliability Based Design, describes different sources of uncertainty and the concepts of Reliability Based Design together with an review of previous research in the field.

Section 2: Probability, aims to refresh the readers memory on the subject of statistics and probability theory.

Section 3: Geostaistics, gives an summary of the geostatistics and random fields.

2.1 Reliability Based Design

Reliability - means to what degree a measurements or calculation can be accurate. This "degree" also called *precision*, as illustrated in Figure 2.1. In statistics, the accuracy is called *bias* and precision is referred to as *variability*.

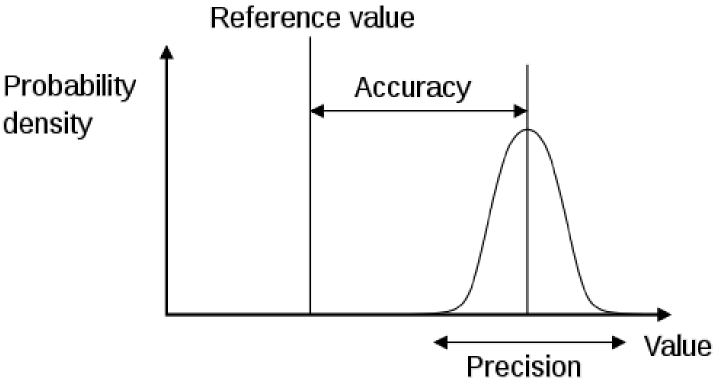

Figure 2.1: The reliability of measurements or evaluated results to a reference value is measured in precision and accuracy, figure created by Pekaje (2017)

One deterministic analysis generates one result, when compared to a reference value, the accuracy can be evaluated. But not the precision. By Reliability Based Design (RBD), both the accuracy and precision of a analysis is possible to measured. In geotechnics, this precision in calculations are often linked to different types of uncertainties.

2.1.1 Sources of Uncertainty in Geotechnics

In Figure 2.2, the three main sources of uncertainties in geotechnics are illustrated (Baecher and Christian, 2003; Vanmarcke, 1977).

The first source of uncertainty is the natural variation or *Aleatoric uncertainty*. The inherent randomness of nature in both time (temporal variability) and location (spatial variability). In soils, it is caused by the natural variation in soil composition and stress history. It is estimated by studying statistical patterns, such as trends and fluctuations, in observed data. This uncertainty is possible to model using mathematical formulations.

The second source of uncertainty is the knowledge uncertainty or *Epistemic uncertainty*. Referring to uncertainty due to lack of information, caused by insufficient measurements or understanding. This uncertainty can be further divided into three underlying subcategories. Namely, the uncertainty in: study site, soil model and model parameters. The

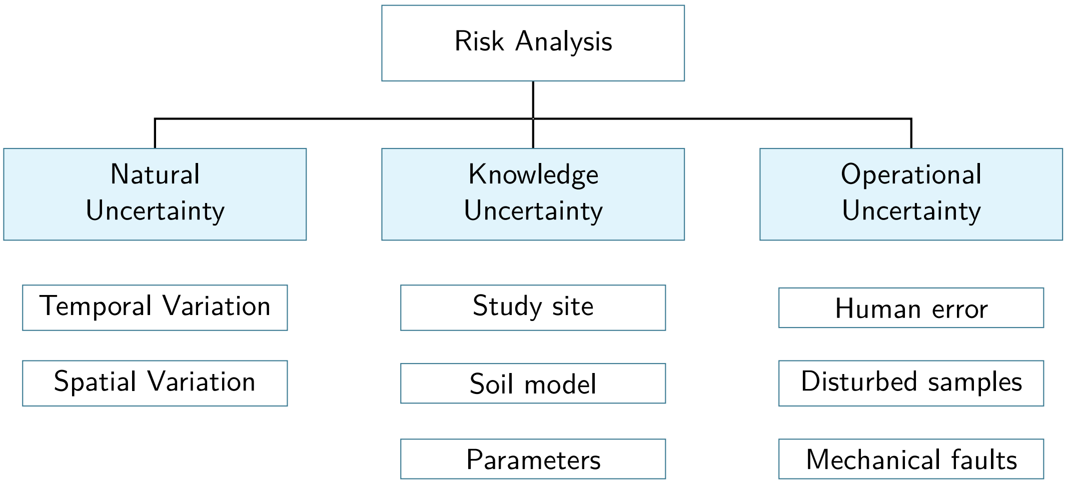

Figure 2.2: Sources of uncertainties in risk analysis after (Baecher and Christian, 2003).

study site, is for example, the lack of information due to restricted numbers of samples or tests on site; measurement errors, due to instrumentation accuracy and systematic measurement errors (bias in testing method) or unrepresentative samples. Model uncertainty is referring to how well the mathematical models is describing a real physical behavior. In geotechnics, this could be the approximations made by a soil models to real soil behaviour. Finally, the last subcategory refers to parameter evaluation. The statistical uncertainty in data handling and parameter estimation. For example, inconsistency on site or measured data and statistical assumption.

The third source of uncertainty, is due to imperfections in measurements caused by the "human error". A example of this is sample disturbance. But also faults in construction or machinery. This source of uncertainty is in most cases the main source of damage according to Blaut (1982) in Schuppener and Heibaum (2011).

This thesis primarily deals with the first type of uncertainty, the inherent natural variability. It can be modelled using random field theory but before going deeper into theoretical aspects, a short summery is given of pioneering work in the field together with some probabilistic methods.

2.1.2 Earlier Research

In 1971 was the international conference *Application of Statistics and Probability in Soils and Structural Engineering* held in Hong Kong, an pioneering "milestone" according to Réthàti (1988). This since from this conference described a large number of statistical working methods regarding soil variation. In the following years more progress was made regarding spatial risk analysis and spatial variations. In the work by Vanmarcke (1977) the concepts of spatial variation and methodology through random field theory by autocorrelation is presented. It can be seen as starting point in this specific field. Another notable study on spatial variation is Soulié et al. (1990) where the spatial variation of undrained shear strength on a clay deposit was estimated using ordinary kriging interpolation.

There is a great number of contributors to to field of today. But, Baecher and Christian (2003); Fenton and Griffiths (2008) is considered the two state-of-the-art books in RBD in geotechnics.

2.1.3 Probabilistic Models

A stochastic or *probabilistic* model is used to estimate *approximately* what will happen. The word *stochastic* comes from the Greek *stokhastikos* meaning "aim at or guess" (Kobayashi et al., 2012).

Before a soil model can be made, a site investigation has to be performed. With enough in-situ field tests the parameter can be estimated with statistics. The soil samples gives additional information, a signal of sorts, regarding the spatial variation of these values. When a proper site investigation have been carried out, calculation can be performed.

In Figure 2.3 a comparison between a deterministic and probabilistic models are given. A deterministic model uses one single characteristic value for the calculation and generates one single result, in stability problems for example an Factor of Safety (FOS). Probabilistic models can be divided into two types: models with and without consideration of spatial variation. *Without* consideration of spatial variability, are models sometimes also referred to as *simple* probabilistic models since only the statistics (mean and variance) of samples are considered but not the spatial variation. Examples of such models are the First and Second Order Reliability Method (FORM/SORM) (Baecher and Christian, 2003) . *With* consideration of spatial variability are models also referred to as *advanced* probabilistic models. One example is RFEM which takes in accounts of both the statistics and the spatial variation thorough random field theory (Fenton and Griffiths, 2008).

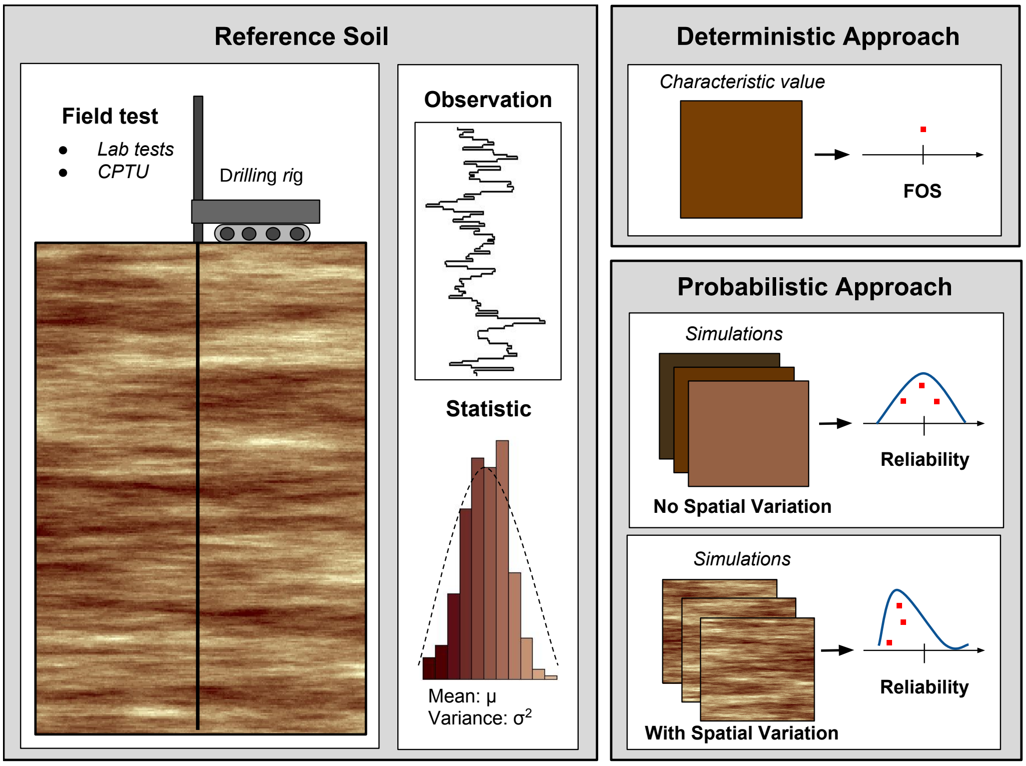

Figure 2.3: Comparison between: one deterministic analysis and two probabilistic analysis with and without spatial variation taken in account

In this thesis, spatial variability is taken in account by an RFEM model. In order use the RFEM for analysis, a random field has to be created, something not familiar to all engineers. However, before elementary knowledge of some statistics is needed and will hence be described in the next section.

2.2 Probability

The term *probability* refers to the chance of an *Event* A to happen. The probability of event A is denoted $P(A)$ and is any number satisfying $0 \leq P(A) \leq 1$.

2.2.1 Discrete Random Variables

A discrete Random variable (RV) usually denoted X only take discrete values $(x_1, x_2, \dots)$ for instance 5, 6 or 7. The RV is generally defined as a real-valued random function $X(\omega)$ that generates a outcome or *elements* ω from its *sample space* Ω. The RV is described by Equation 2.1 and illustrated in Figure 2.4.

$$X(\omega) = \omega \qquad \Omega = [\omega_1, \dots, \omega_N] \qquad A = [\omega : condition] \tag{2.1}$$

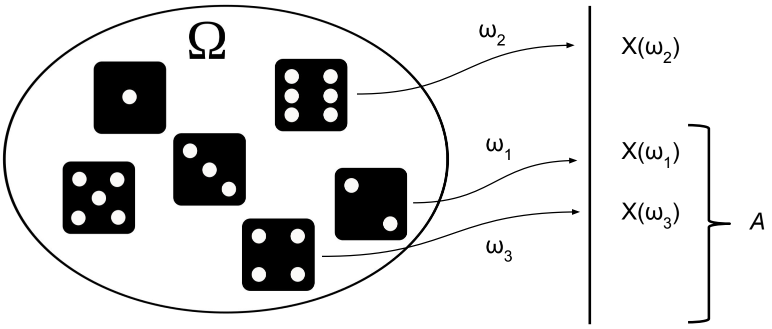

Figure 2.4: A random variable $X(\omega)$ with three random samples.

$f_x(x)$ is call the *probability mass function* (PMF) for a discrete variables. The PMF contains the probability for any element in RV sample space. It is used to calculate the probability for P(A) for any event A such that

$$P(A) = \sum_A f_x(x) \qquad x \in A \qquad 1 = \sum_x f_x(x) \tag{2.2}$$

Example: Let the RV X be a normal dice. X have six possible outcomes from the samples space $\Omega = [1, 2, 3, 4, 5, 6]$. One RV simulation or one dice roll $X(\omega)$, generates one random sample ω. What is the probability for $P(A) = 6$? The solution is simply:

$$P(A) = \frac{1}{n} \sum_{i=1}^{n} f_x(x) x_i = \frac{1}{6} \sum_{i=1}^{N} 1 = \frac{1}{6} \tag{2.3}$$

2.2.2 Continuous Random Variables

For a continuous random variable X, the PMF is integrated over its sample space turns to the *probability density function* PDF, denoted as

$$PDF(x) = f_x(x) \tag{2.4}$$

The probability of the event A is written as,

$$PDF(A) = \int_A f_x(x) dx \qquad x \in A \tag{2.5}$$

The PDF over the entire domain is always equal to one,

$$\int_{-\infty}^{\infty} PDF(x)dx = 1 \tag{2.6}$$

A RV sample space is can be described by the *cumulative distribution function* CDF denoted $F_x(x)$. The CDF can be defined as the area under the PDF.

$$CDF(x) = F_x(x) = \int_x F_x(x)dx \tag{2.7}$$

As the CDF increases it approaches 1 from 0,

$$F_x(-\infty) = 0 \qquad F_x(\infty) = 1 \tag{2.8}$$

The probability of x in the interval (x_1, x_2) is computed accordingly,

$$PDF(a \leq x \leq b) = \int_b^a f_x(x)dx = CDF(b) - CDF(a) \tag{2.9}$$

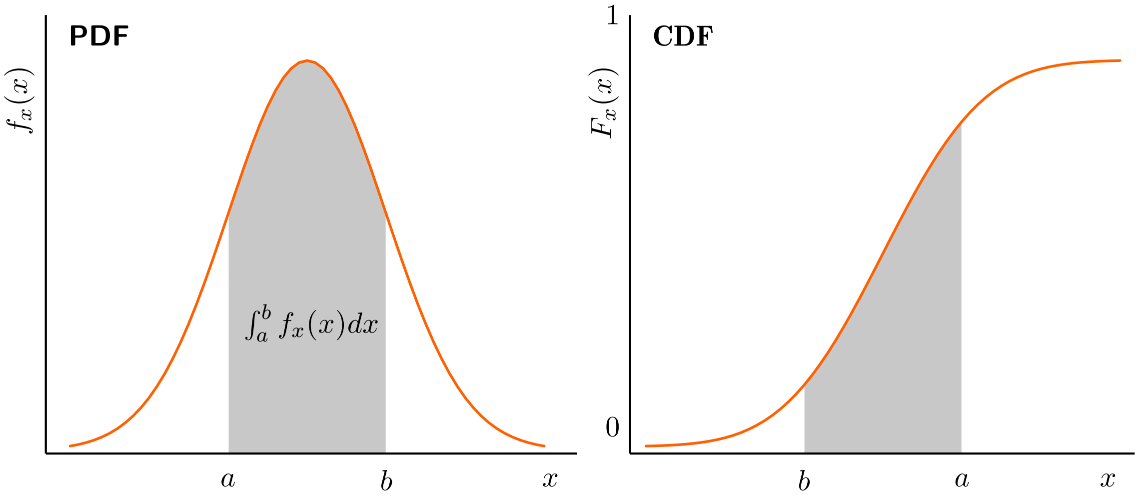

Figure 2.5: Probability Density Function (left) and Cumulative distribution function (right) of a normal distribution.

2.2.3 Moments of a Distribution: Mean and Variance

To fit random variables to field data it is necessary to describe the data statistically. This is done by a statistical measurement called moments. Through moments a RV can be fitted approximately. The two most common measures are the *central tendency* (1:st moment) and *variability* the (2:nd moment). The univariate moment of degree k is defined as:

$$M_k = \frac{1}{N}\sum_{i=1}^{N}[x_i - E(x)]^k = E[x - E(x)]^k \tag{2.10}$$

Where N is the total number of elements and $E(X)$ refers to expected value of X, for $k = 1$ the mean is equal the expected value hence often denoted as $E(x) = \mu_x$.

The first moment, defines the central tendency of the distributions. It is measured in mean (expected value) or median. For discrete and continuous distributions the mean is denoted as μ_x respectively and defined as:

$$M_1 = \frac{1}{N}\sum_{i=1}^{N} x_i = \mu_x = E(X) \qquad \text{if X is discrete} \tag{2.11}$$

$$M_1 = \int_{-\infty}^{\infty} x f(x) = \mu_x = E(X) \qquad \text{if X is continuous} \tag{2.12}$$

the *sample mean* $\bar{x}$ is using a subset n from N, and defined as

$$\bar{x} = \frac{1}{n}\sum_{i=1}^{n} x_i \tag{2.13}$$

The *median* is sometimes used over mean for robustness, since the mean is more sensitive for extreme values in the distributions. The median is defined as the point which divides the distribution in the middle.

The second moment, variability, is a measure of the distributions spread. The *variance* is denoted as σ_x^2 and defined by

$$M_2 = \frac{1}{N}\sum_{i=1}^{N}(x-\mu_x)^2 f(x)_x = E[(X-\mu_x)^2] = \sigma_x^2 = Var(x) \tag{2.14}$$

$$M_2 = \int_{-\infty}^{\infty}(x-\mu_x)^2 f(x) = E[(X-\mu_x)^2] = \sigma_x^2 = Var(x) \tag{2.15}$$

The standard deviation σ is equal to the square root of the variance $\sigma = \sqrt{Var(X)}$. Standard deviation is also used for a measurement of spread. But is influences by the distribution mean. A normalized measure of variation is the *coefficient of variation v* which represents the ratio between the standard deviation and the mean.

$$v = \frac{\sigma}{\mu} \tag{2.16}$$

2.2.4 Covariance and Correlation

Two random variables might influence each other, in so called Covariance (CoV). The covariance is central for random field theory, which is explained later in section 2.3. One typical example of covariance in geotechnical engineering is between the soil parameter shear strength c and friction angle ϕ. The variation between these two are correlated such that a low value of c effects the probability of ϕ to also be low.

The relationship between the covariance of two random variables X and Y and their joint probability distribution $f_{xy}(x,y)$, is defined as

$$\begin{aligned} Cov(X,Y) &= E[(X-\mu_x)(Y-\mu_y)] \\ &= \sum_x\sum_y (x-\mu_x)(y-\mu_y)f_{xy}(x,y) \\ &= \int_{-\infty}^{\infty}\int_{-\infty}^{\infty}(x-\mu_x)(y-\mu_y)f_{xy}(x,y)dxdy \end{aligned} \tag{2.17}$$

In Figure 2.6, two random variables X and Y are shown with the covariance in-between them marked in orange. The covariance of two variables X and Y can also be computed with the known mean of μ_x and μ_y as following

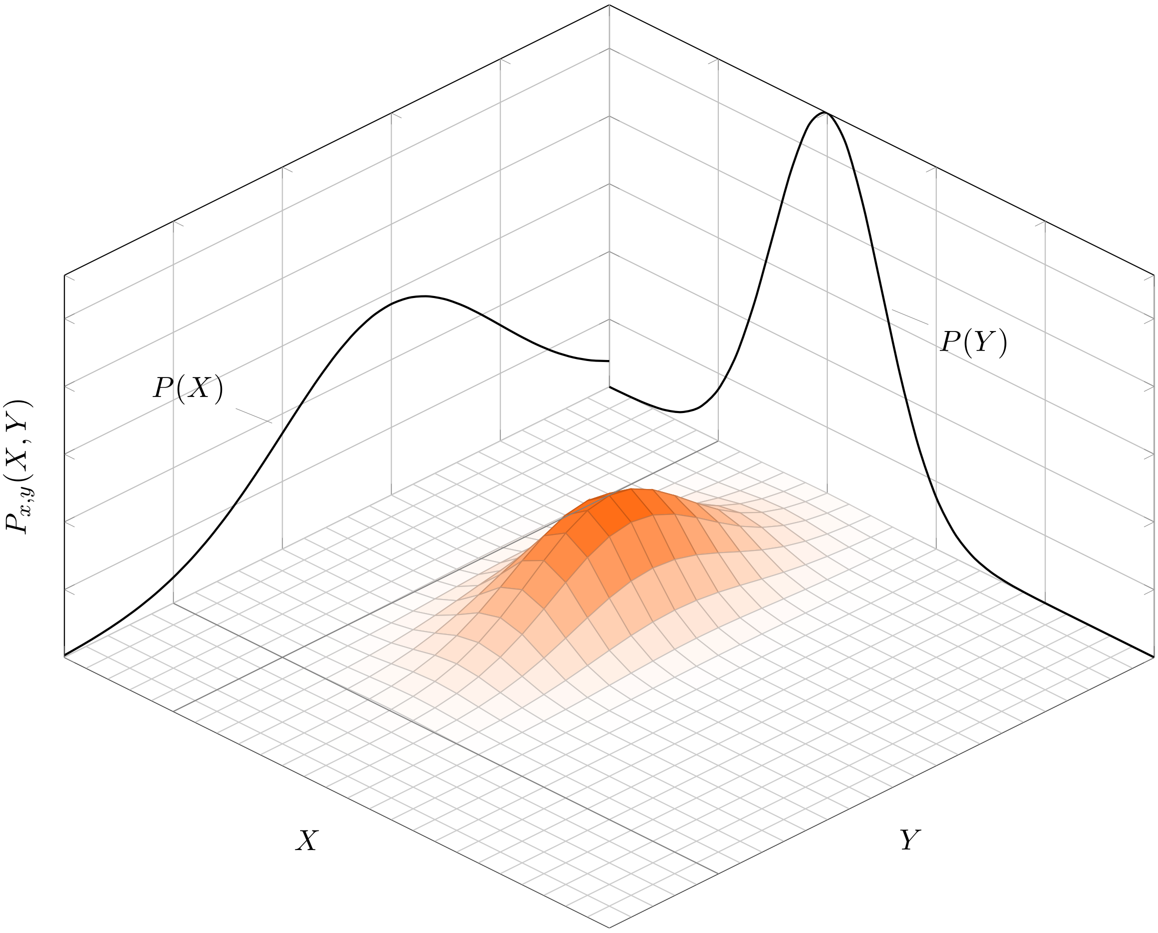

Figure 2.6: Figure of two random variables X and Y and their bivariate probability density function $f_{xy}(x, y)$

$$Cov(X, Y) = E(XY) - E(X)E(Y) = E(XY) - \mu_x \mu_y \tag{2.18}$$

Statistical correlation means that two variables may showing causal dependence by each other. One measurement for correlation between X and Y is the Pearson correlation coefficient ρ_{xy} and is defined as

$$\rho = \frac{COV(XY)}{\sqrt{Var(X)Var(Y)}} = \frac{COV(XY)}{\sqrt{Var(X)Var(Y)}} \tag{2.19}$$

Lets assume that for some observed values y is depend on a single variable x. One way to test this hypothesis is by a *linear regression model.*

2.2.5 Linear Regression Model

Observe the measured data in Figure 2.7. The hypothesis is that observed data points are correlated such that y_i is dependent on x_i and follow a hypothetical trend line. By regression the measurements is approximate by *simple linear* or *polynomial regression model* defined as:

$$y = \alpha + \beta_1 x + \epsilon \qquad y = \alpha + \beta_1 x + \beta_2 x^2 + \epsilon \tag{2.20}$$

where y is the target variable, or the *dependent variable*; x the explanatory variable or the *independent variable*; α, β the regression parameters (intercept and slope) and ϵ the random error or *residual.*

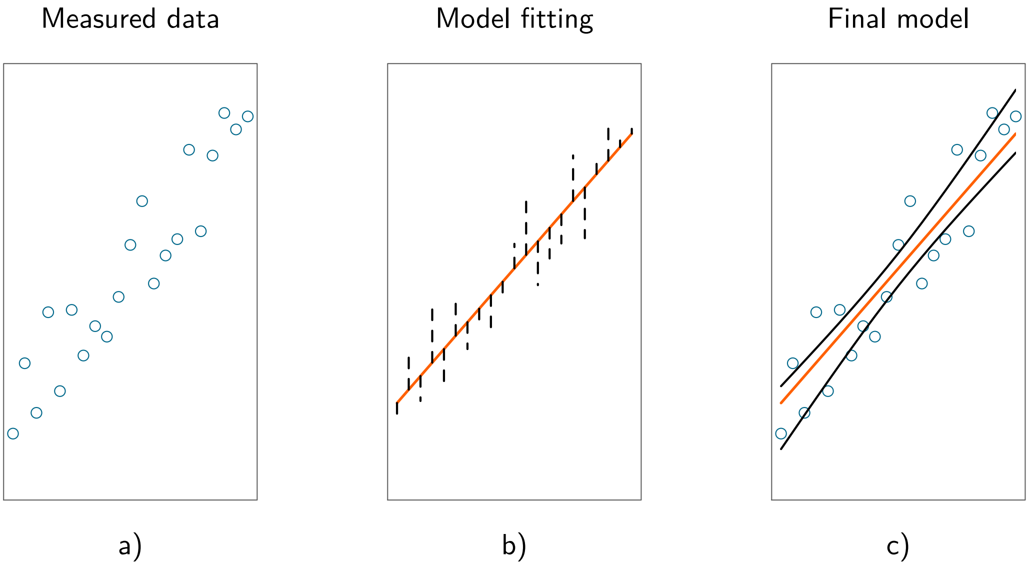

Figure 2.7: An example of fitting a simple linear regression model to measured data: a) observed data points , b) Fitted linear model with $min(RSS)$ residual distance in black and c) shows the final model with a 95% confidence interval boundries.

The fit the parameters α, β is by least squares; the methods minimizes the total area made by the distance from the line to the measured point in square, we call this area the *Residual Sum of Squeres* (RSS) and define it as:

$$RSS = S(\alpha, \beta) = \sum_{i=1}^{n} (y_i - \alpha - \beta x)^2 = \sum_{i=1}^{n} \epsilon^2 \tag{2.21}$$

It's important to understand that the parameters α, β are optimized in such way that it minimizes the RSS, the residual distance are illustrated in figure 2.7b).

2.2.6 Spatial Interpolation

Spatial data is any value at a specific point in space given by coordinates in 2D (x, y) or 3D (x, y, z). Spatial interpolation techniques is used to predict a unsampled point Z^* between two or more data points. Interpolation techniques can be divided into two groups, *local* and *global techniques* (Laaha, 2016).

Local techniques estimates the unsampled point by only take in account of data points closest to it. Examples of such techniques are: linear interpolation, triangulations and the nearest neighbor method. Global techniques on the other hand uses all the data for the value prediction, examples of such techniques are: Inverse Distance Weighting (IDW) and Kriging interpolation.

All techniques uses *weights* for prediction. A weight is a real-value $\lambda \in [0, 1]$ given to a data point Z_α to predict the value of an estimate Z^*. Let n be the number of spatial data points; the interpolation of Z^* is then the sum of local or global data points Z_α times each weight λ_α.

$$Z^* = \sum_{\alpha=1}^{n} \lambda_\alpha Z_\alpha \tag{2.22}$$

A important condition for the weights is that they are *unbiased.* This means that λ_α is equal to the estimate λ^* at any data point, denoted as $E(Z_\alpha^*) = E(Z_\alpha)$, which in turn also means that sum of the weights $\sum_{\alpha=1}^{n} \lambda_\alpha$ is equal to 1, such that over or undershooting i restricted.

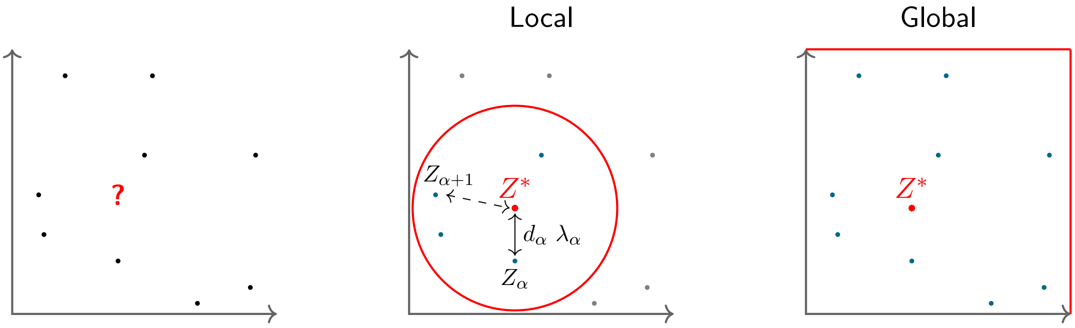
Local

Global

a) b) c)

Figure 2.8: Illustration of 2D interpolation; where a) shows the unsampled point Z^* being estimated by both local b) and global c) interpolation; where Z_α is the measured data point and d_α its distance from Z^*.

Figure 2.8 shows spatial data and examples of local and global interpolation techniques. Weights are usually calculated as a function of either distance or area between the data points Z_α and the unsampled point Z^*. A simple local interpolation technique such as triangulations, gives the weights λ to the data points Z_α based only on the distance between it and the unsampled point Z and Z^*, let us denote this distance d_α, see figure 2.8. The weights is given by the relative linear distance, $\lambda = d_\alpha / \sum d_\alpha$. Clearly, this is not a optimal method since it does note take in account all the sampled data. Over and down-shooting also arise when points are clustered.

An alternative method is to use regression technique over the domain of study and estimate both the predicted value and the uncertainty.

2.3 Geostatistics

Kriging: " A collection of generalized linear regression techniques for minimizing an estimation variance defined from a prior model for a covariance" (Olea, 1991, p.41)

The kriging method, named by Matheron after Krige, optimizes the interpolation by using linear regression on the unsampled point Z^* (Wackernagel, 2003). From the regression technique the method gives both an estimate and variance in the point of consideration. The estimate on the unsampled point Z^* is defined as

$$Z^*(x) = \sum_{\alpha=1}^{n} \lambda_\alpha Z(x_\alpha) = \sum_{\alpha=1}^{n} \lambda_\alpha \gamma(x - x_\alpha) \tag{2.23}$$

Where γ is the semivariance function or *variogram* is central in kriging interpolation. It defines the covariance between the unexampled value and estimate depending on distance. These two values are refers to as the start or head value x_i and the end or head value y_i. The semi-variogram value for N samples, considering one lag h is defined as:

$$\gamma(h) = \frac{1}{2N(h)} \sum_{i=1}^{N(h)} (x_i - y_i)^2 \tag{2.24}$$

where; N, is the number of pairs, x_i, the start or tail value of the pair i and the end or head value.

Figure 2.9 shows the correlation parameters of the spatial structure in relationship to the variogram. The correlation parameters are the following: the priori variance or *nugget value* C_0. Which is the variance do to experimental error or other causes in the evaluation of sample values. The constant variance value or *Sill value* C and the distance a until the variogram reaches a constant variance refers to as the *range* or *correlation length.*

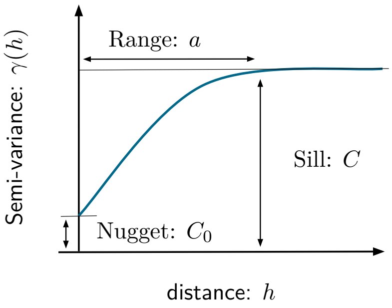

Figure 2.9: Definitions of the correlation parameters in the variogram

One way to explain why the semivariogram is used is by the considering the two signals in Figure 2.10. They have the same statistics, mean and variance, but are clearly different. A new statistical term is needed in order to distinguish them, the correlation length, which is defined through the variogram.

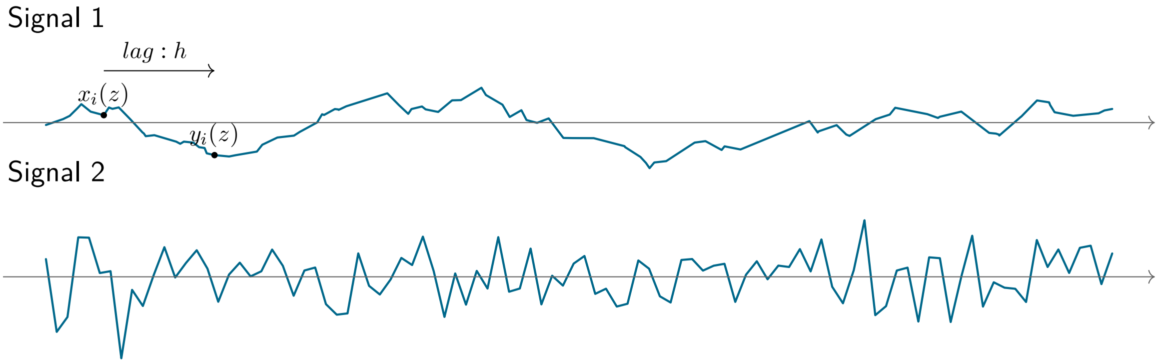

Figure 2.10: Two signals: with and without spatial correlation

In Figure 2.11, the signal semivariograms are shown. These are generated from evaluating the semi-variance value from all possible distance lag pairs. In the figure, the variogram vales are marked with circles. Signal 1 show low semivariance on short distances, compared to Signal 2 which shows constant high semivariance values on all distances. The conclusion from this image is that Signal 1 is spatially correlated within a distance, while Signal 2 is show no sign of correlation. The distance where sampels are correlated is referred to as range, *correlation length* or *scale of fluctuation* denoted a or θ.

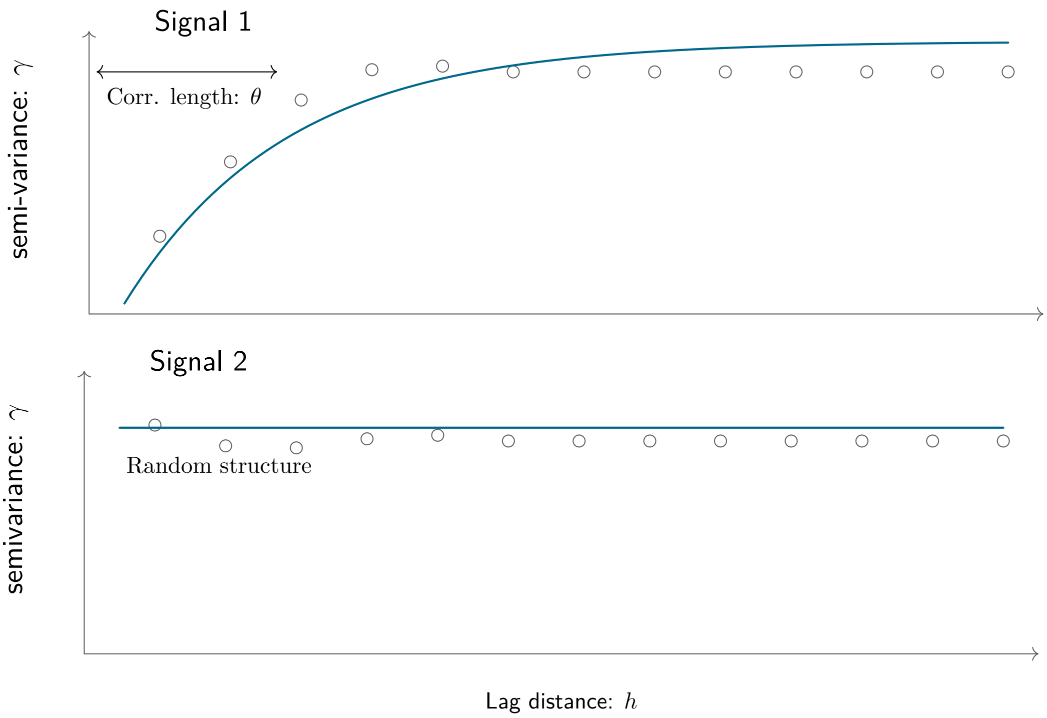

Figure 2.11: Two variograms to corresponding signal: showing spatial correlation and a random structure

In order to simulate a Gaussian random field a theoretical correlation model is fitted to the empirical data. When simulating a random field, *the degree of anisotropy* ξ is often used (Fenton and Griffiths, 2008). Figure 2.12 shows the influence of ξ on the random field simulation. It is defined a the ratio between the horizontal and vertical correlation length denoted

$$\xi = \frac{\theta_h}{\theta_v} \tag{2.25}$$

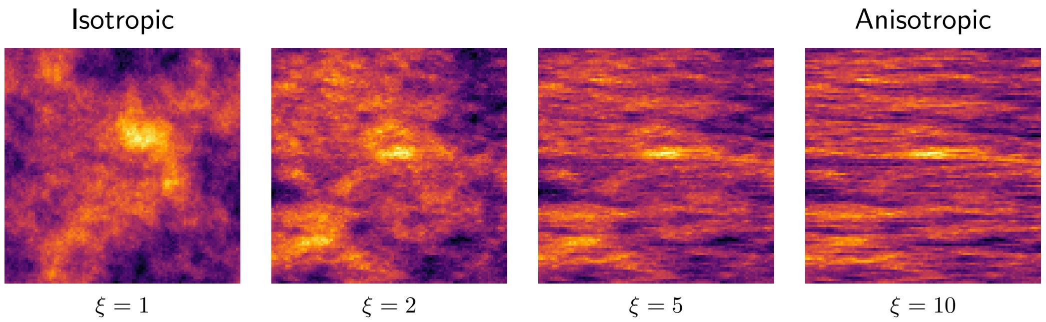

Figure 2.12: The influence of different degrees of anisotropy on the Gaussian random field

3 Methods

3.1 Outline

The method outline can be described in four stages as illustrated in Figure 3.1.

Stage 1: In the first stage, the geology of the Perniö test embankment is described together with selected soil models and corresponding parameters. From samples the initial OCR data is statistically evaluated and checked for fulfilling the criteria of normality and stationarity, which is necessary for the subsequent kriging interpolation.

Stage 2: In this stage, anisotropic kriging interpolation is performed by a theoretical variogram model fitting to estimated pair values on site. The interpolation is done using the *geoR* library in R which generates two rasters; one with the variance of the OCR and one with the estimate. These two raster are then used to simulate the RFEM raster in the next stage.

Stage 3: The two kriging rasters are used to generate three deterministic rasters; one maximum, minimum and estimate raster and 500 RFEM rasters. The deterministic and probabilistic rasters are used in the next stage as input for the FEM analysis.

Stage 4: In the last stage, each deterministic and RFEM raster for the embankment are calculated by FEM in PLAXIS 2D. A Python script parses the RFEM raster to the PLAXIS code for Monte Carlo simulations that calculate embankment failure load and pre-failure deformations. These results are exported and saved for further post processing.

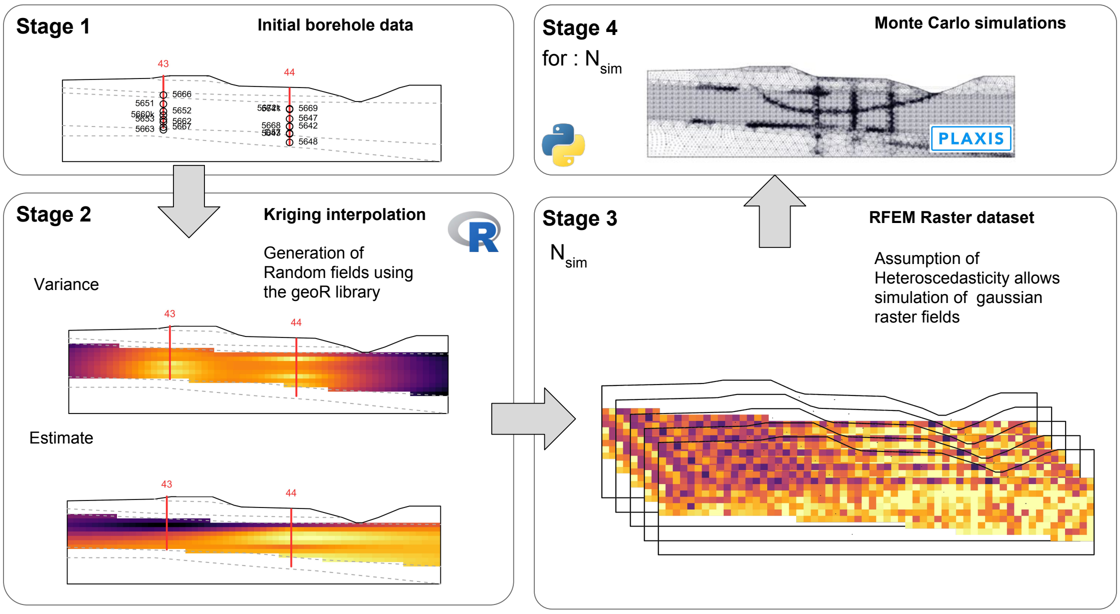

Figure 3.1: Figure of the method procedure in four stages

In the following sections, the methodology is further elaborated. The first stage in the procedure is to characterise Perniö test site and summarise the initial borehole data.

3.2 Study Site

3.2.1 Perniö Test Embankment

In October 2009, a full-scale embankment failure test was conducted on an old railway embankment, located close to the city of Perniö in South West Finland (Lehtonen et al., 2015). A map of the geographic location together with more maps of the site is found in Appendix A.

The test embankment was built on initiative of Tampere University of Technology and the Finnish Transport Agency, simulating a fully loaded train, bringing the embankment to failure. The failure test procedure was conducted by loading the carts on top of the embankment, which failed by an undrained creep rupture mechanisms 28 hours after the 87 kPa load step. For a complete description of the test is referred to (Lehtonen et al., 2015; Lethonen, 2011).

Figure 3.2: Perniö test embankment with the placement of loading carts and measuring instrumentation before the test procedure (Lehtonen et al., 2015)

Figure 3.2 shows the Perniö test embankment; to the left, the loading carts position; and to the right, the excavated ditch to steer the failure direction. In-between, inclinometers are installed to measure pre-failure displacements and failure mode. A map of all instrumentation locations is shown in Appendix B whereas all relevant measurements for this study are described further in Section 3.5.

3.2.2 Site Conditions

Figure 3.3 shows the cross-section of study together with the soil profile. The section is 30 m wide and 8 m in height. The initial ground surface is at approximately + 8.2 m elevation and the ground water level in the area is located at 1.5 m below the soil surface (Lehtonen et al., 2015). Boreholes 44 and 43 are used to evaluate soil layering and properties for the site.

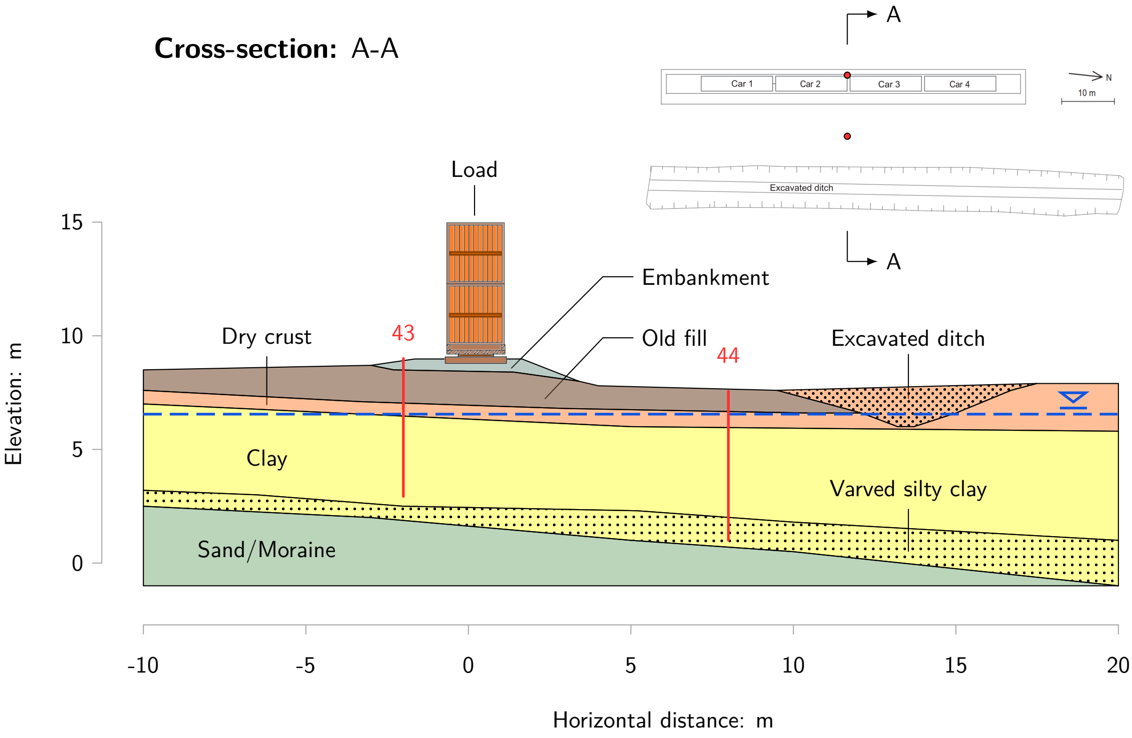

Figure 3.3: The cross-section of study at Perniö test embankment, together with subsoil layers and the position of borehole 43 and 44.

3.2.3 Constitutive Soil Models and Parameters

From Borehole 44 and 43, samples are collected for further laboratory testing which in turn are used to evaluate the model parameters. For the full site investigation map, see Appendix B. A summary of characteristic constitutive soil models and parameters, for all six layers in the soil profile, are summarised in Table 3.1.

1: The embankment, consists of sand and gravel with a thickness of 1 m (Lehtonen et al., 2015). The saturated unit weight is assumed to be $\gamma_{sat} = 19kN/m^3$. A Mohr-Coulomb model with the stiffness of $E' = 40kPa$ was used together with a effective friction angle of $\phi' = 30$ and cohesion of 5 kPa for improving numerical convergence.

2: The old fill, has the same charismatics as the embankment but is 1.5 m in thickness and a stiffness of $E' = 30kPa$.

3: The crust, consists of 0.6-0.9 m weathered clay and a unit weigh of $\gamma_s at = 18kN/m^3$. A hardening soil model set for the layer with typical stiffness parameters: $E_{50}^{ref\prime} =$

$25kPa$ and $E_{ur}^{ref\prime} = 75kPa$ to fit overconsolidated clay crust. The cohesion was estimated to be 70 kPa.

4: The clay, which is the layer this Thesis will focus on, consists of 3.5- 4.5 m of normally consolidated soft clay. The saturated unit weight is $\gamma_{sat} = 15kN/m^3$. The soft soil model was used with the stiffness parameters of $\lambda^* = 0.2$ and $\kappa^* = 0.0015$, evaluated according the procedure presented in Gras et al. (2017).

5: The varved silty clay, is approximately 1.5 m thick and consists of soft clay with inclusions of silt. The soft soil model is also used for this layer, but with slightly stiffer parameters compared to the main clay layer $\lambda^* = 0.2$ and $\kappa^* = 0.0015$.

6: The Sand/Moraine, is located at bottom and consists of densely packed glaciers moraine with and is estimated to be 3-4 m thick before bedrock.

Table 3.1: Material model parameters set for subsoil layers

Layers		**Embankment**	**Sand/Fill**	**Crust**	**Clay**	**Varved Clay**	**Sand/Moraine**	**Unit**
General								
Material model	$Model$	Mohr-Coulomb	Mohr-Coulomb	Hardening soil	Soft Soil	Soft Soil	Mohr-Coulomb	
Drainage type	$Type$	Drained	Drained	Drained	Undr. (A)	Undr. (A)	Drained	
Soil unit weight above phreatic level	γ_{unsat}	16	16	15	14	14	16	kN/m^3
Soil unit weight below phreatic level	γ_{sat}	19	19	18	15	16	19	kN/m^3
Inital void ratio	e_{init}	0.5	0.5	0.5	2.2	2.2	0.5	-
Parameters								
Secant stiffness	E_{50}^{ref}	-	-	25	-	-	-	kN/m^2
Tangent stiffness	E_{50}^{oed}	-	-	25	-	-	-	kN/m^2
Unloading stiffness	E_{ur}^{ref}	-	-	75	-	-	-	kN/m^2
Power of stresslevel dependency	m	-	-	0.5	-	-	-	-
Stiffness	E'	40	30	-	-	-	20	kN/m^2
Poissin's ratio	ν	0.3	0.3	-	-	-	0.3	kN/m^2
Mod. compression index	λ^*	-	-	-	0.2	0.15	-	-
Mod. swelling index	κ^*	-	-	-	0.015	0.02	-	-
Effective cohesion	c'_{ref}	5	5	70	1	1	1	kN/m^2
Effective friction angle	ϕ	35	33	30	30	30	36	°
Dilatancy angle	ψ	0	0	0	0	0	0	°
Advanced: Set to default		Yes	Yes	Yes	Yes	Yes	Yes	-
Groundwater								
Data set		USDA	USDA	USDA	USDA	USDA	USDA	
Model		Van Genuchten	Van Genuchten	Van Genuchten	Van Genuchten	Van Genuchten	Van Genuchten	
Soil type		Sand	Sand	Clay	Clay	Silty clay	Sand	
<2μm		4	4	70	70	13	4	%
2μm - 50 μm		4	4	13	13	13	4	%
50μm - 2 mm		92	92	17	17	17	92	%
Set to default		Yes	Yes	Yes	Yes	Yes	Yes	-
Horizontal permeability	k_x	7.1	7.1	0.047	0.047	0.004	7.1	m/day
Vertical permeability	k_y	7.1	7.1	0.047	0.047	0.004	7.1	m/day
Initial								
K0 determination	-	Automatic	Automatic	Automatic	Automatic	Automatic	Automatic	
Overconsolidaion ratio	OCR	1	1	2	Raster	1.4	1.4	-
Preoverburden pressure	POP	-	-	-	-	-	-	kN/m^2

3.2.4 Spatial Variation of OCR

All parameters are pre-defined except the spatial variation of apparent preconsolidation pressure, which in this Thesis is estimated by a random field. The apparent preconsolidation pressure, σ_p, is often expressed by the over consolidaion ration OCR, which is the ratio between the σ_p and the in-situ effective vertical stress, σ'_v:

$$OCR = \frac{\sigma_p}{\sigma'_v} \tag{3.1}$$

In Figure 3.4 the spatial variation of estimated OCR is illustrated with corresponding boreholes. A total of 17 samples was taken from the two borehole close to the embankment; 8 samples from borehole 43 and 9 samples from borehole 44. The OCR values from borehole 43 indicates a slightly more over consolidated clay compared to 44. Possibly due to the old embankment effecting this location.

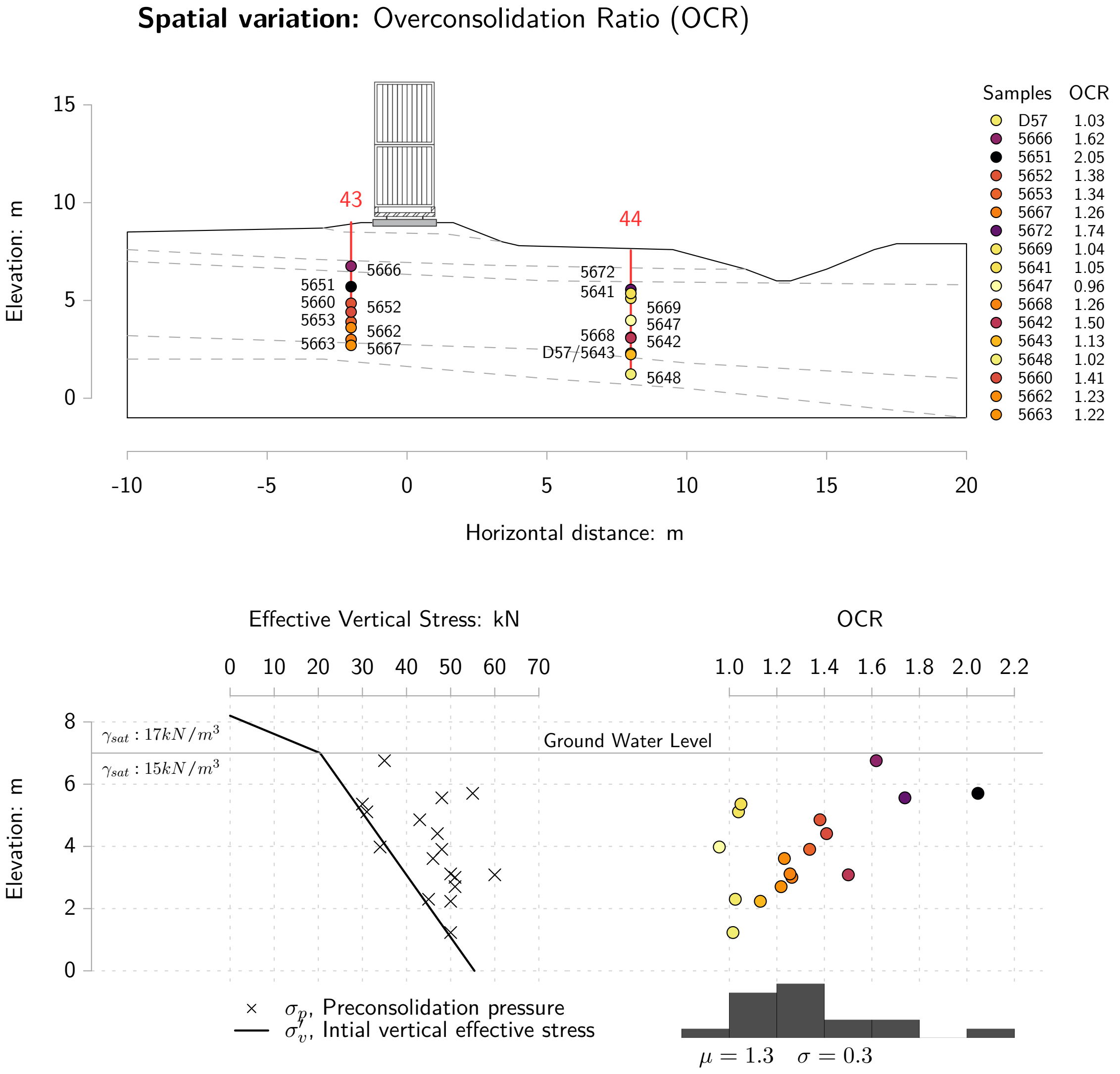

Figure 3.4: The spatial variation of OCR in borehole 43 and 44 on site and the estimation of OCR as the ratio of in-situ effective vertical stress, σ'_v, preconsolidaion pressure, σ_p.

The OCR was estimated through σ'_v and σ_p as illustrated in Figure 3.4. The σ_p, is evaluated from 17 oedometer test. and for σ'_v following condition are assumed: a ground water level, at +7 m elevation; ground level,at +8.2 m and soil unit weights, above of $\gamma_{sat} = 17\,kN/m^3$ and $\gamma_{sat} = 15\,kN/m^3$, below and above 7m elevation.

Figure 3.4 shows that the OCR for the clay is ranging widely between 1 and 2, making the selection of a single characteristic value hard. The OCR distribution is close to normally distributed, with the global mean, $\mu = 1.3$; and standard deviation of, $\sigma = 0.3$. All sample with estimated values are summarized in table in Appendix C.

Before performing kriging interpolation, the OCR data has to fulfill two necessary criteria; namely normality, meaning that the data is normally distributed; and stationarity, refering to the first and the second moment is constant all over the data domain. The data is found to be both normally distributed, as illustrated in the QQ-plot in Figure 3.5, and stationary, giving no signs of significant trends. Fulfilling these two criteria, it is possible to perform kriging interpolation on the OCR data.

3.3 Kriging Interpolation

The kriging interpolation is performed using the R library package "GeoR" provided by Ribeiro and Diggle (2016). The spatial correlation of the OCR data is estimated using the semi-variogram, denoted as

$$\gamma(h) = \frac{1}{2N(h)} \sum_{i=1}^{N(h)} (x_i - y_i)^2 \tag{3.2}$$

where; N, is the number of pairs, x_i, the start or tail value of the pair i and; y_i, the end or head value.

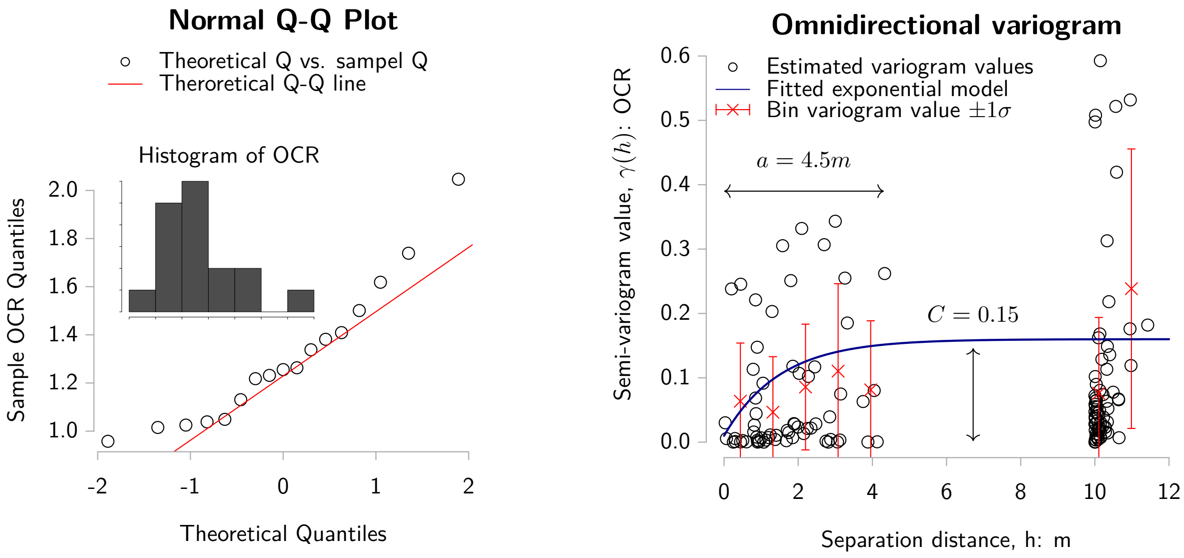

Figure 3.5: Normallity check of OCR Data through a QQ-plot and omnidirectional variogram of OCR data showing the exponential model fit.

In Figure 3.5, the resulting semi-variogram values ,$\gamma(h)$ are plotted in a omnidirectional variogram. These values are binned (red), where the bin μ and σ is fitted with a exponential semi-variogram model (blue). The exponential model is defined by the covariance parameters: range a and a positive variance contribution value or sill value C.

$$\gamma(h) = C(1 - e^{-3h/a}) \tag{3.3}$$

In this thesis, the covariance parameters used for the fitted exponential variogram model is a range of $a = 4.5$ and sill of $C = 0.15$.

The scale of fluctuation θ, is defined as the range of distance wherein measurements are correlated. Based on the relationship provided by Vanmarcke (1984), the scale of fluctuations can be estimated from the exponential model range a.

$$\theta = \frac{2}{3}a \tag{3.4}$$

The vertical scale of fluctuation, θ_v, refers to the correlation length in the vertical direction. The range a is derived from the variogram seen in Figure 3.5. It is in vertical direction since the variogram parameter a is fitted to the points in the range of 0 to 5 m, corresponding to only vertical pairs. Given the value $a = 4.5$, the vertical scale of fluctuation is simply $\theta_v = 3m$.

The horizontal scale of fluctuation, θ_h, could not be estimate from the variogram in the same manner. this due to lack of horizontal pairs with different separation distances and more borehole data is required to evaluate θ_h from the variogram properly.

A different way to estimate θ_h is by the degree of anisotropy, ξ, which is the ratio between the horizontal and vertical scale of fluctuation, defined as

$$\xi = \frac{\theta_h}{\theta_v} \tag{3.5}$$

Knowing, θ_v and ξ , would make it possible to derive θ_h. For this thesis, a reasonable ξ was adopted from another study site with similar conditions.

In the study by Soulié et al. (1990), the correlation ranges for undrained shear strength, S_u, was estimated to 3 m and 10 m. Resulting in the degree of anisotropy of $\xi = 10$. Since there is a relationship between S_u and σ_p, and hence also OCR, similar spatial variation are assumed for the Perniö site. When adopting the degree of anisotropy of $\xi = 10$ and knowing $\theta_v = 3$, it results in $\theta_h = 30$.

Table 3.2 summerises the covariance parameters a and C, to the fitted exponential variogram model $\gamma(h)$ and the anisotropic conditions, $\xi = 10$, used for simulating the kriging random fields.

Table 3.2: Summary of Perniö variogram parameters

Exponential varigram model			
Parameters	**Symbol**	**Value**	Unit
Vertical Range of correlation	a	4.5	m
Sill value	C	0.15	-
Degree of Anisotropy	ξ	10	-
Vertical Scale of Fluctuation	θ_v	3	m
Horizontal Scale of Fluctuation	θ_h	30	m

3.3.1 Homogeneous Random Field

The first kriging model is a *homogeneous* random field, assuming the *same* correlation length in all directions, i.e $\xi = 1$.

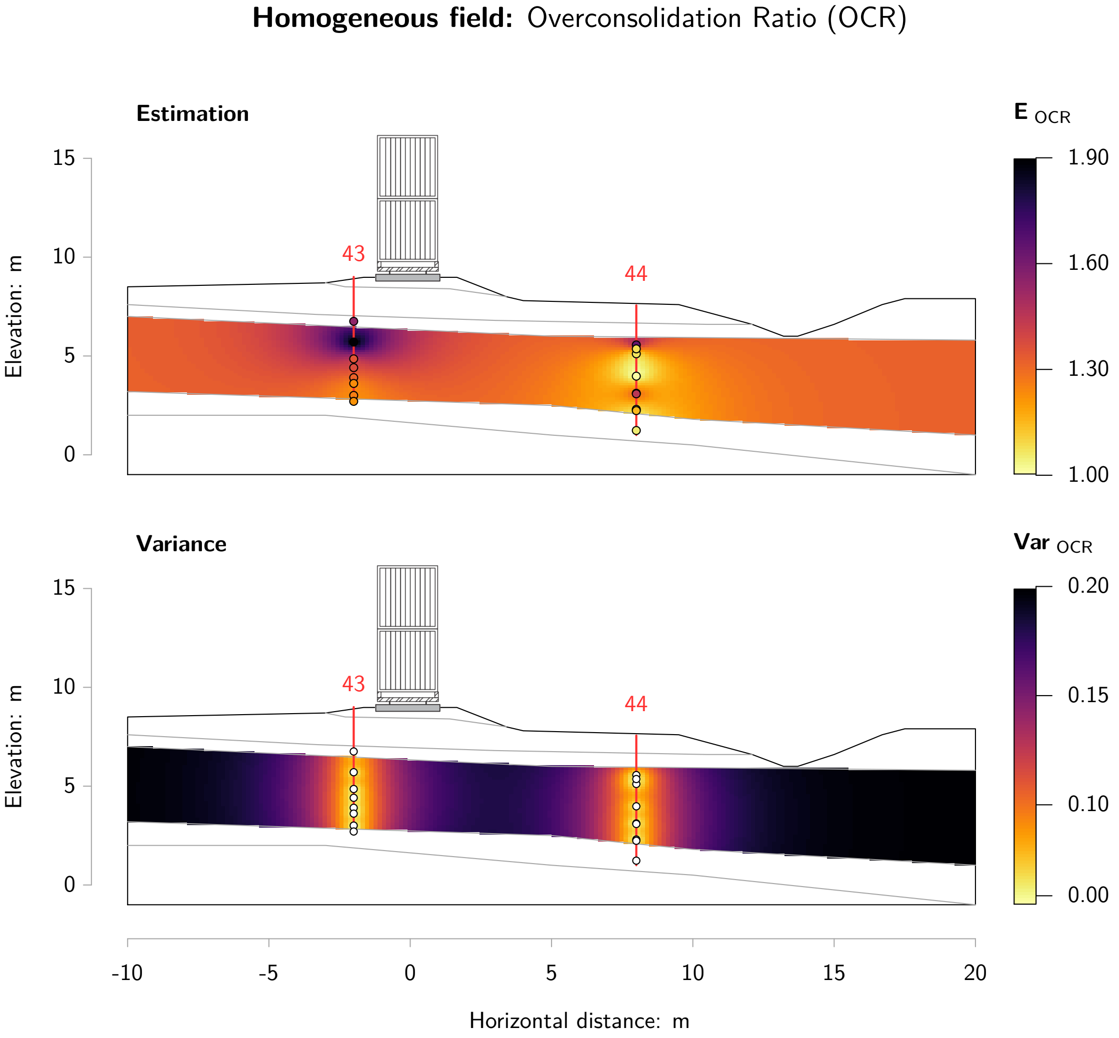

Figure 3.6: Figure of two homogenous random fields $\xi = 1$: illustrating the OCR estimation (top) and variance (bottom) over the domain of study

In Figure 3.6, the estimate and variance of OCR is simulated by a homogeneous random field exhibiting the same amount of variation in all directions. The theoretical exponential variogram model infuses the variation of OCR in both the estimate and variance raster. Consider the estimation raster; the values within the correlation distance, $\theta_v = \theta_h = 4.5$, are influenced by the measured OCR value. Further away, the value increases and ultimately, at set the correlation distance of 4.5 m, converges to global OCR mean $\mu = 1.3$. The uncertainty or variance is influenced in a similar way. The variance is smaller closer to the measured OCR values and increases by the distance.

The homogeneous model predicts the OCR for homogeneous conditions. But, as mentioned earlier: clays are to some degree anisotropic and variate differently by direction.

3.3.2 Anisotropic Random Field

The second kriging model is a *anisotropic* random field with *different* correlation length depending on direction, a 10 times difference is assumed, $\xi = 10$.

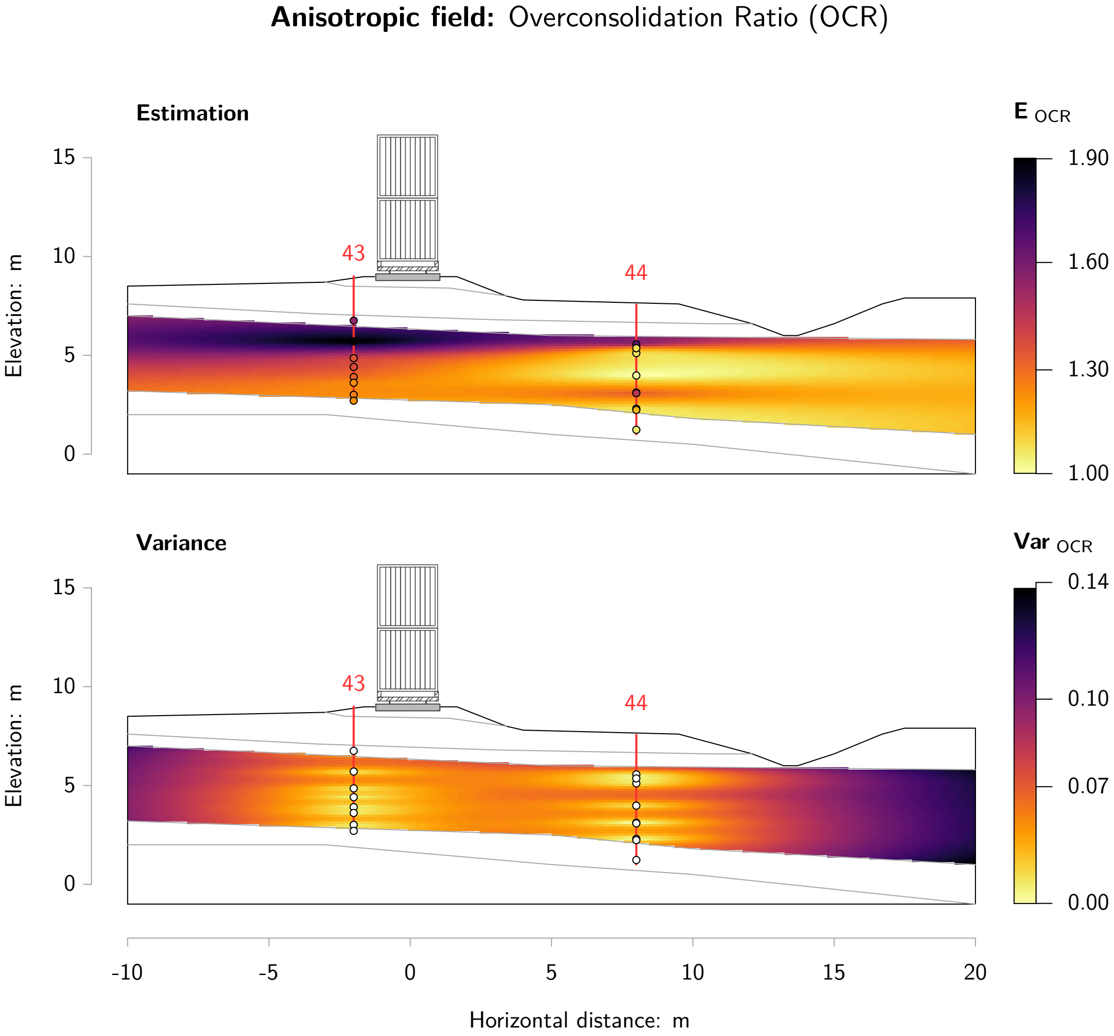

Figure 3.7: Figure of two anisotropic random fields, where $\xi = 10$: illustrating the OCR estimation (top) and variance (bottom) over the domain of study

The estimate and variance of OCR is first simulated a homogeneous random field, in order to simulate a degree of heterogeneity of $\xi = 10$, the fields are transformed in the horizontal direction by the same degree, generating this anisotropic raster. In Figure 3.7, the estimate and variance show in this case a difference in the variation depending on direction imposed by the degree heterogeneity.

In this thesis, the anisotropic OCR model was used for the FEM calculation of: embankment failure load and displacements. From these rasters, both deterministic and stochastic datasets are created for the analysis, these are further explained in the following section.

3.4 Spatial Estimation of OCR Used for Analysis

In this section, the OCR input for deterministic and probabilistic analysis are described. The anisotropic model from the kriging interpolation is used, but due to software limitations, it is necessary to down-scale the raster to the resolution of 60×12, which is equivalent to 0.5×0.5 meters in real size.

Figure 3.8 illustrates the down-scaled estimate of OCR, E_{OCR}, and standard deviation, σ_{OCR}. Compared to Figure 3.7, it is possible see the effects due to lower resolution.

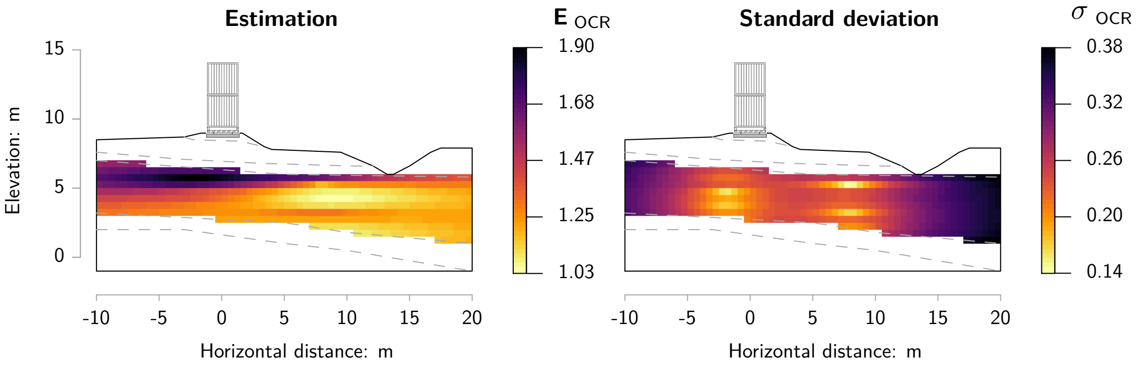

Figure 3.8: The down-scaled anisotropic random fields

3.4.1 Deterministic analysis

Since one single deterministic analysis only generates one result, it is not possible to estimate the uncertainty in parameters by one single analysis. However, by taking a lower and higher bound of the uncertain parameter, and perform a *sensitivity analysis*, corresponding results will indicate a range of the parameter uncertainty. Having the anisotropic kriging model, it is possible to perform a sensitivity analysis with spatial variation taken in account.

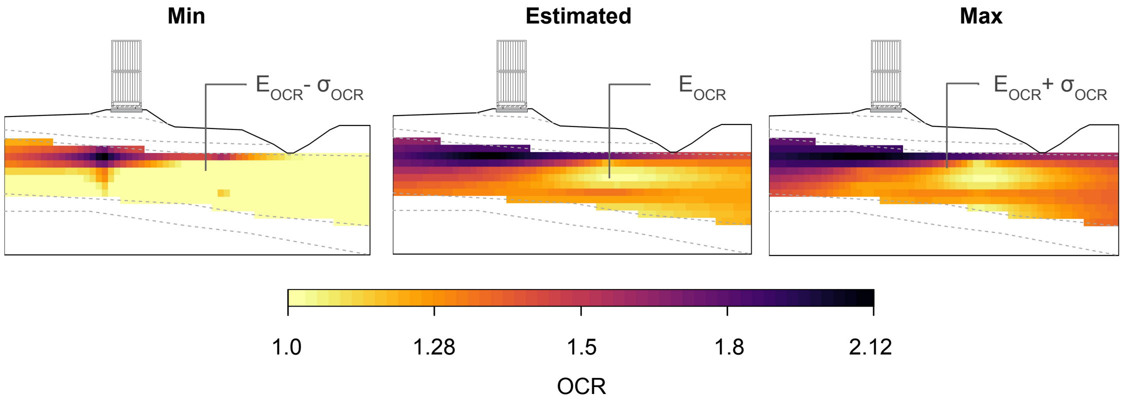

Figure 3.9: OCR datasets used for the determinsistic analysis

In Figure 3.9, the three datasets for the deterministic analysis are illustrated: a minimum value raster, mean or estimated raster, and maximum raster. The calculation of each raster are as follows: $Min = E_{OCR} - \sigma_{OCR}$, $Max = E_{OCR} + \sigma_{OCR}$ and $Estimate = E_{OCR}$. It is important to notice that values of $OCR < 1$ is adjusted to $OCR = 1$.

The three determinstic rasters may give the range of the uncertainty, but not give the probability, for this more simulations are needed in a so called probabilistic approach.

3.4.2 Probabilistic analysis

The dataset for the probabilistic model is assumes stationarity over the domain. Giving the stationary condition, a total of 500 RFEM rasters are simulated by implementing each cell *independently* with a normally distributed random number, generated according to $N(E_{OCR}(x,y), \sigma_{OCR}(x,y))$, where the E_{OCR} and σ_{OCR} are the parameters illustrated in Figure 3.8 .

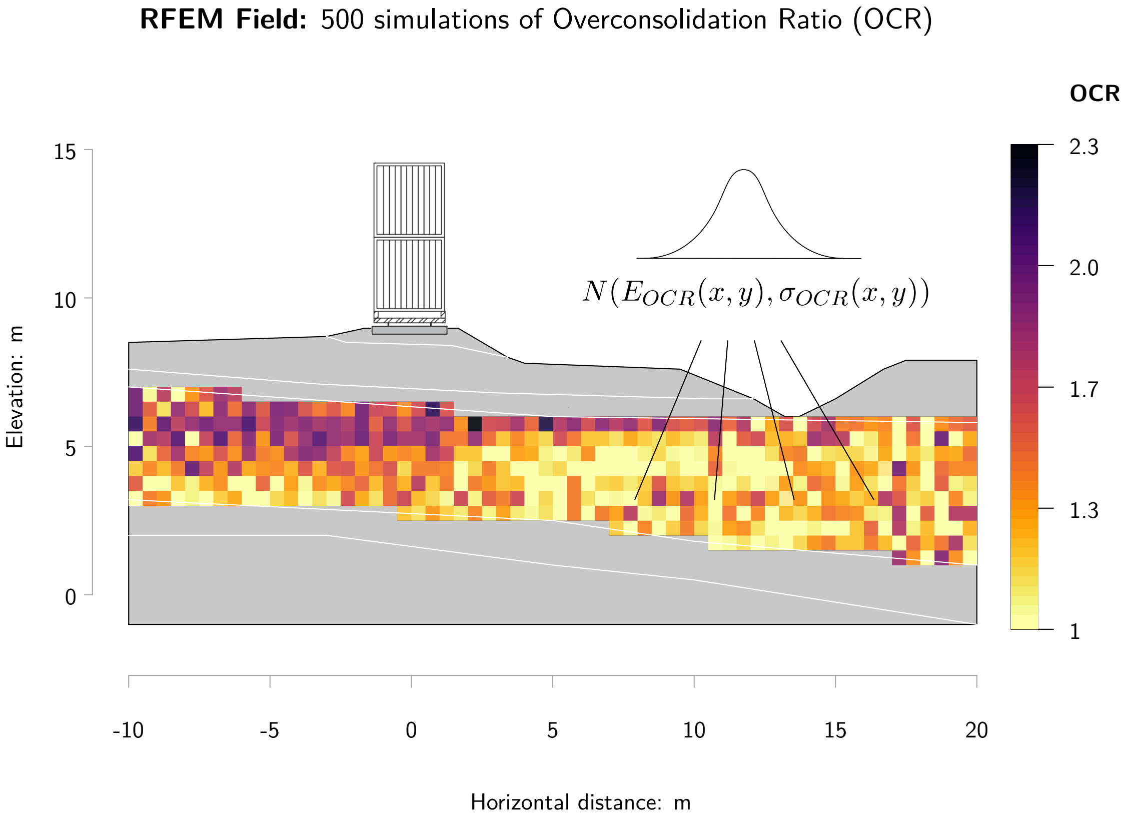

Figure 3.10: A RFEM field of size 60 × 12 masked to the clay layer of study

Figure 3.10 shows a RFEM raster simulation. Note that it is possible to see the influence of E_{OCR} by the higher value of OCR below the embankment and also the variance σ_{OCR} generating a scatter of variation over the domain.

By 500 simulations, 500 possible scenarios are created from the spatial probability of the variogram. In the last stage, the presented OCR dataset are calculated using Monte Carlo simulations in within an finite element framework.

3.5 Numerical model

In order to calculate the embankment failure load, deformations and failure mechanism, a numerical FEM model is created using PLAXIS 2D.

In Figure 3.11, the numerical model is illustrated. The model is 30 m long and 8 m of height, the boundary conditions are fixed at bottom and horizontally fixed on the sides. The mesh is made from 3826 elements and 30913 nodes, refined around three inclinometers used for the benchmarking of displacements, and also along a potential failure line. A uniform load, Q, is placed on top of a 2.5 m wide stiff plate assigned stiffness parameters:

$EA = 5 \times 10^6\,kN/m$ and $EI = 8500\,kNm^2/m$, which is equivalent to a concrete slab of thickness 0.15 m.

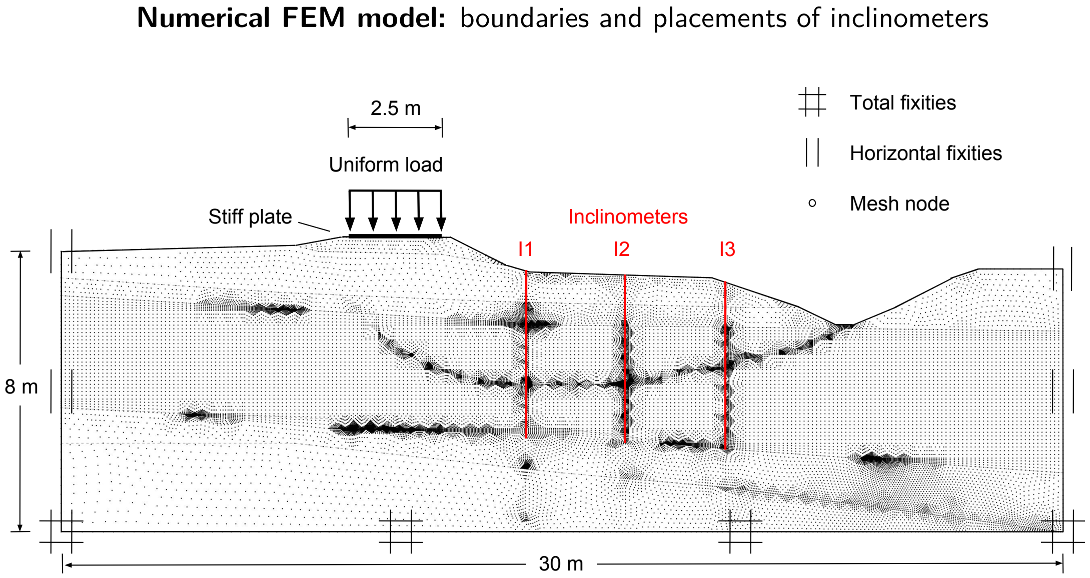
Numerical FEM model: boundaries and placements of inclinometers

Figure 3.11: Geometry and bound conditions of the numerical model with inclinometers used for benchmarking

Each simulation with an OCR raster set generates a embankment failure load and deformation. The implementation of spatial variation raster into PLAXIS is made through remote scripting using Python. The script is based on previous work by Akbas (2015) but improved in order to take in account of spatial variation. The script generates the model by first defining the geometry. Then, cutting out raster-size cells from the geometry and assign these with a unique material model corresponding to the OCR value given by the kriging raster. Lastly, calculations phases are set up according to the procedure of the Perniö test embankment before analysis. For more details regarding geometry and material models see Appendix XXX.

In Figure 3.12, the test procedure of Perniö embankment according the loading scheme presented in (Lehtonen et al., 2015) and corresponding model phases are presented. The phases simulate the test procedure which was conducted by loading the containers on the top of the embankment gradually with sand. During the first three hours a load of 21 kPa was created. At t=3:20 the experiment was halted overnight. The experiment resumed next morning at t=16:45 and loaded with approximately 5.5 kPa/h until reaching maximum load (87 kPa) at t=28:04.

In Table 3.3, model phases are summarized. The phases can be divided into two groups: Before the experiment (Phase 1-4) and after (Phase 5-). Before the test, the site was constructed; first, the initial ground level is modelled; then, the ditch is excavated and the new embankment built; and finally, there is a consolidation phase of 5 days before the test loading procedures. The test procedure is modelled by a loading phase from 0 to $24\,kPa$ in one single step, then the embankment is consolidate for 12 hours. The second loading stage is again by 11 steps from 24 to $79\,kPa$. The step-wise increment is used for the evaluation of failure mechanism which will be explained further later. If the embankment have not failed by phase 18, the loading continues until failure.

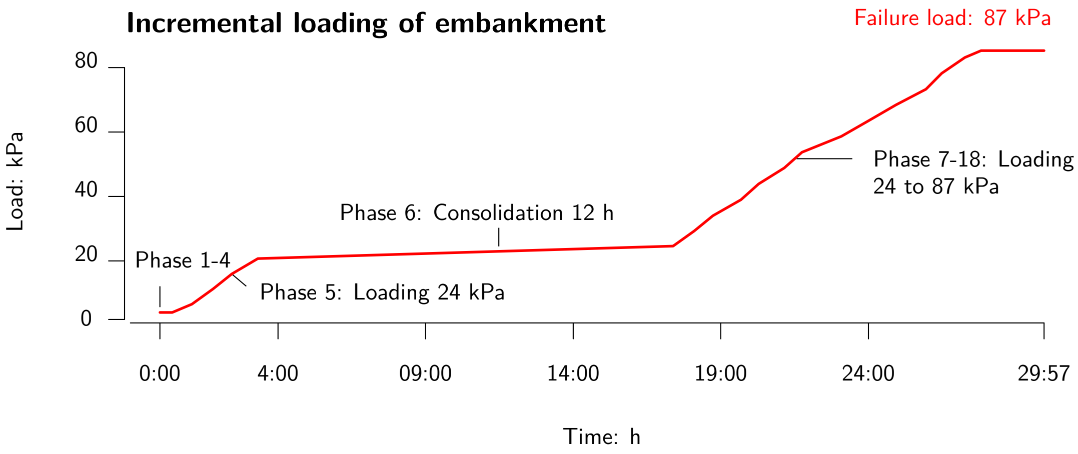

Figure 3.12: Measure loading procedure and model phases for Perniö test embankment

Table 3.3: PLAXIS phases

Calculation phases		
	Name	**Description**
phase 1	initial phase	groundlevel at +8 m
phase 2	excavation of ditch	
phase 3	new embankment	
phase 4	consolidation	5 days
phase 5	loading	$Q = 24\,kPa$
phase 6	consolidation	0.5 days
phase 7-18	loading	$Q = 24 + 5.7 \times i\,kPa*$
phase 19	loading until failure	$Q = Q_{F}ailure$
When Embankment fails, $Mstage < 1$		
safty phase	determine failure mechanism	

* i current phase

3.5.1 Estimation of Failure load, deformations and failure mechanism

For each simulation: failure load, deformations and failure mechanism are evaluated from last phase. The failure load is calculated using Mstage and phase load, Q, such that

$$\textbf{Failure load:} \qquad F = Mstage * Q \tag{3.6}$$

At failure the horizontal and total displacements are also saved. In order to estiamte the failure mode, a PLAXIS "safety phase" (strength reduction phase) is added onto the last stabile phase. For example, if phase 10 fails, a safety phase is added after phase 9. From the safety phase the total displacements are used to estimate size of the failure mass. The failure mass is defined as the area containing all nodes with a total displacements value larger then the 10th percentile. The area is estimated through a Riemann sum with 100 segments over the domain.

4 Results

The embankment is analysed in terms of: embankment displacements and failure load using both a deterministic and probabilistic model. The deterministic models refers to the three FE simulations corresponding to the OCR raster input (min, estimated and max) described in Section 3.4.1. The probabilistic model refers to the 500 RFEM simulations corresponding to the OCR raster dataset described in Section 3.4.2.

In Figure 4.1, one deterministic result of pre-failure horizontal displacements and failure mechanism, determined by the estimated OCR raster, E_{OCR}, is shown. The displacements U_x, are in the range of 0 to 27 mm, and largest in the underlying clay layer on the bottom right side of the embankment. These are compared to data from inclinometers I1,I2 and I3. The embankment failure mode is also shown. The failure load is 89 kN for E_{OCR}, creating a rotational mass movement with a total area of 51 m^2.

In the following Sections, the results of: displacements, failure load and failure mechanism, will be further elaborated for all models.

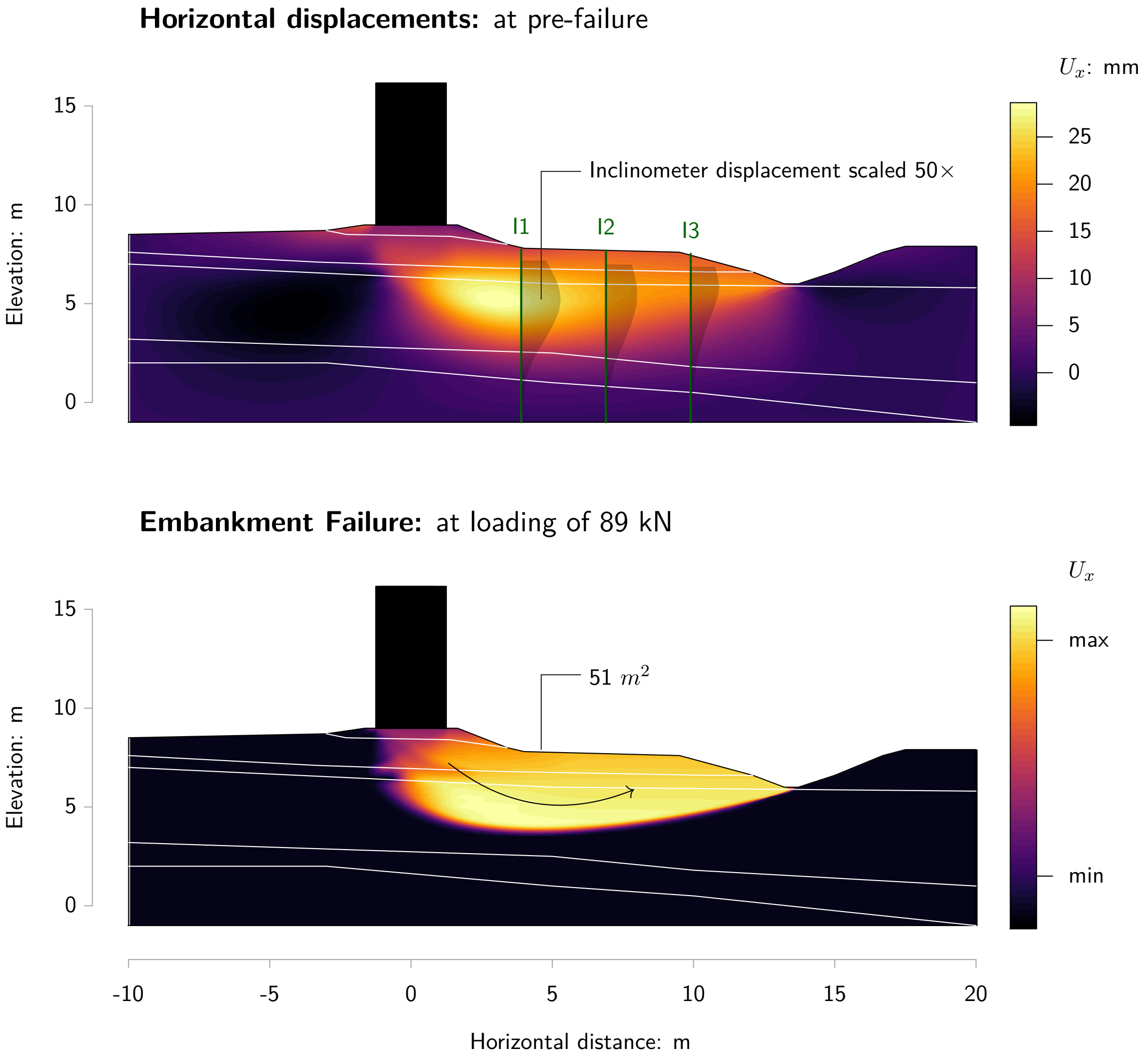

Figure 4.1: Horizontal displacements and failure mechanism for the Perniö test embankment from the deterministic analysis of E_{OCR}

4.1 Horizontal displacements

In Figure 4.2, observed horizontal displacements from inclinometers I1, I2 and I3 are compared to the deterministic and probabilistic analyses. The observed values, (black lines) are all from the time of the ultimate load step at t=28:00 until embankment failure (solid black line) at t=29:55. The results in the Figure show that modelled displacements are the largest closer to the embankment at I1 and decreasing with distance in I3. The results of both models agree well with the observed displacements at t=29:35. But due to the undrained creep failure and the use an of the soft soil model that does not incorporate creep the embankment exhibited larger displacements then predicted by the model.

When comparing the results from the deterministic and probabilistic model, it shows that the deterministic model did not capture the uncertainty range as well as the probabilistic model. The variation in displacements for the probabilistic model are closer to the measured data and vary in the range of 10 to 40 mm. The inclination of all lines, however, show similar shape compared to the observed values, which indicate that model deformations are realistically mobilised.

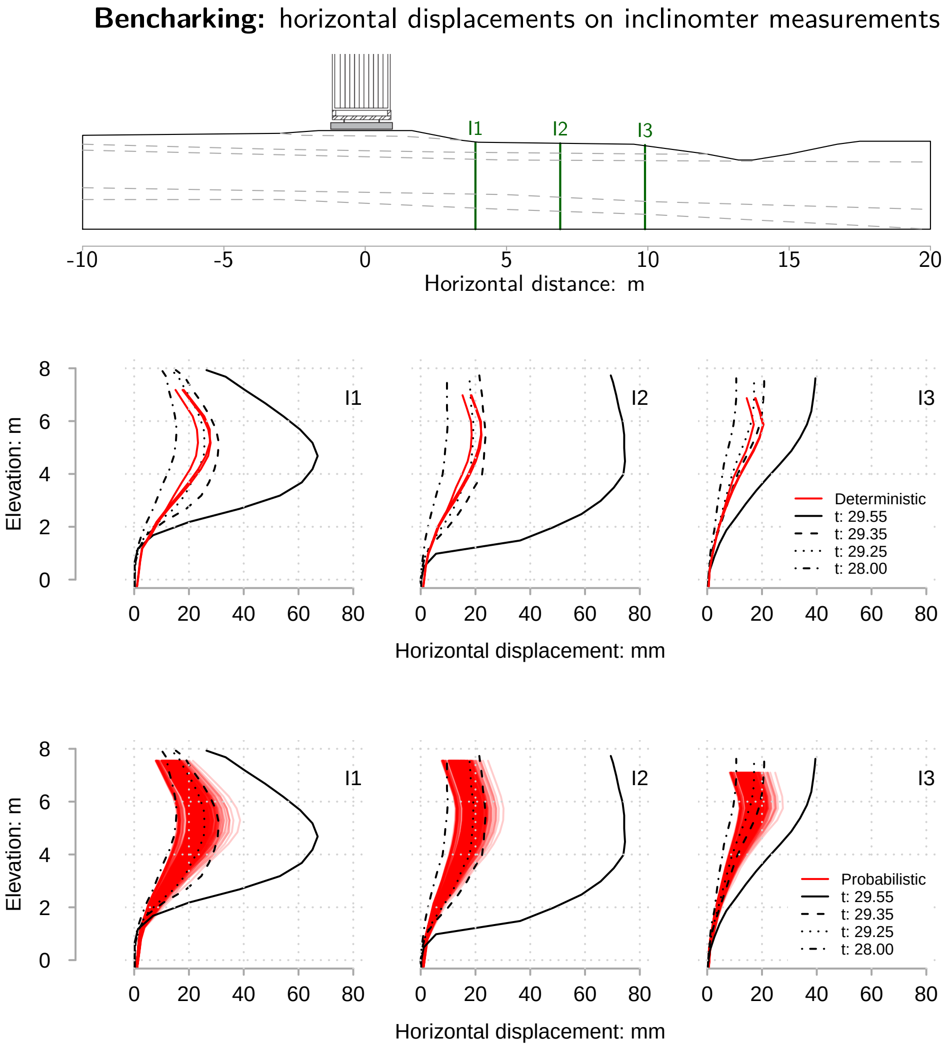

Figure 4.2: Benchmarking of horizontal displacements from deterministic and probabilistic analyses in inclinometer observations

4.2 Embankment Failure load

In Figure 4.3, the probabilistic failure load is compared to the deterministic results (solid black line) and the observed failure load (dashed black line) at $F_{obs} = 86\,kN$. The probabilistic failure load distribution is shown in the histogram and the corresponding probability can be estimated from the cumulative distribution function (CDF). Note that the failure load is ranging from 70 to 105 kPa and is not normally distributed. In the histogram two groups are seen; one around 83 kPa, and the other at 97 kPa. Generally, this is a sign of different failure modes, but for this case it is most likely a sign of bias in raster cell size.

The three deterministic model results are summarised in Table 4.1, and correspond to the OCR raster layers: minimum, estimated and maximum. The minimum OCR raster, min_{OCR}, resulted the lowest failure load, $F_{min} = 81.3\,kN$, and the maximum OCR raster, max_{OCR} , in the maximum failure load, $F_{max} = 99.0\,kN$. This is expected since a low OCR also gives the soil low shear strength. The analysis with the most likely OCR for the embankment, the estimated OCR raster E_{OCR} , fails at $F_{est.} = 88.6\,kN$ and is the closest by all deterministic analyses to real observed value, $F_{obs} = 86\,kN$.

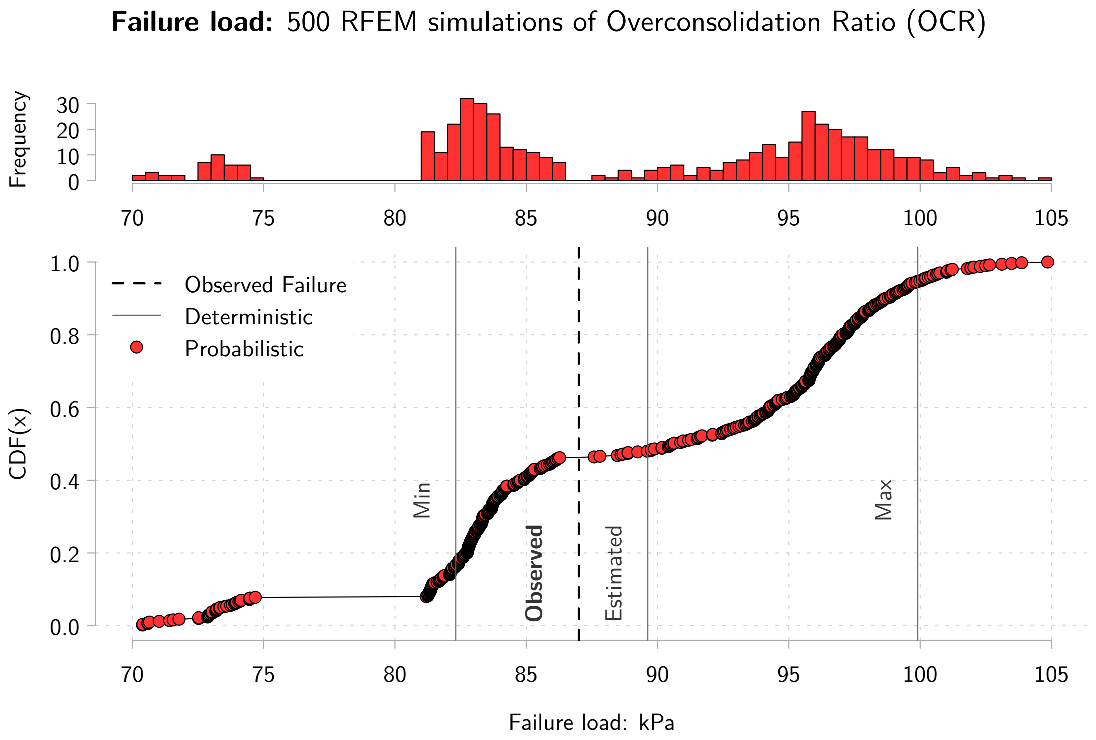

Figure 4.3: Benchmarking of Perniö embankment failure load: Probabilistic approach compared to the deterministic analyses and observed value.

Table 4.1: Summary of deterministic results in Perniö embankment failure load .

Deterministic analysis				
Results	**min**	**estimated**	**max**	Unit
Failure load: F	81.3	88.6	99.0	kN

The deterministic results give a reasonable indication of the range of failure load uncertainty, by incorporating around 80% of all RFEM simulations. The difference in failure load between the deterministic min and max and the estimate, are not the same, but the probability for both models are: $CDF(min) \approx 0.1$ and $CDF(max) \approx 0.9$. This shows that some sign of causality due to probability.

In Figure 4.4, the probabilistic failure load is compared to the work by (Mansikkamäki, 2015) on deterministic analysis using various material models. The observed value $F_{obs} = 86\,kN$ is indicated with the black dashed line and the probabilistic RFEM results statistics is illustrated by the red boxplot. Note that the majority of deterministic FEM results are within the minimum and maximum range of the RFEM analysis. This shows the magnitude of uncertainty due to parameter variation and the hardship in justifiably comparing material models using one single deterministic analysis.

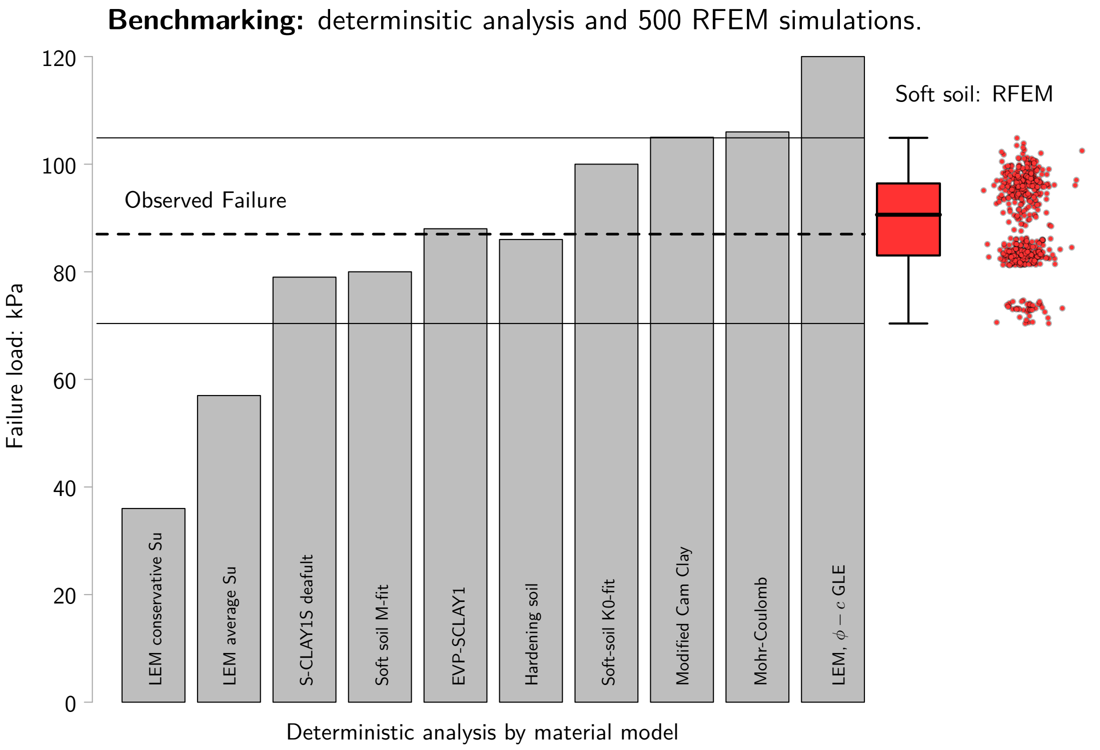

Figure 4.4: Benchmarking of Perniö embankment failure load: Probabilistic approach compared to the deterministic analyses and observed value.

4.3 Failure mechanism

In Figure 4.5, the failure mode of 500 RFEM probabilistic simulations are compared to the field observations presented in Lehtonen et al. (2015). Note that the simulated results (red) are close to the approximated band of shearing, but does not completely reach the same depth. The simulated results exhibit a small variation which increases with depth, but all results show a similar shape. The mass area is also estimated for all simulations, ranging from 48 - 50 m^2 (cross-sectional surface area). A low value of mass area indicates a smaller scale on the failure. However, the differences in resulting areas are not sufficiently large to be different failure mechanism as illustrated in the Figure. Which indicates that the spatial variation of apparent preconsolidation pressure shows no effect on failure mode for the Perniö test embankment.

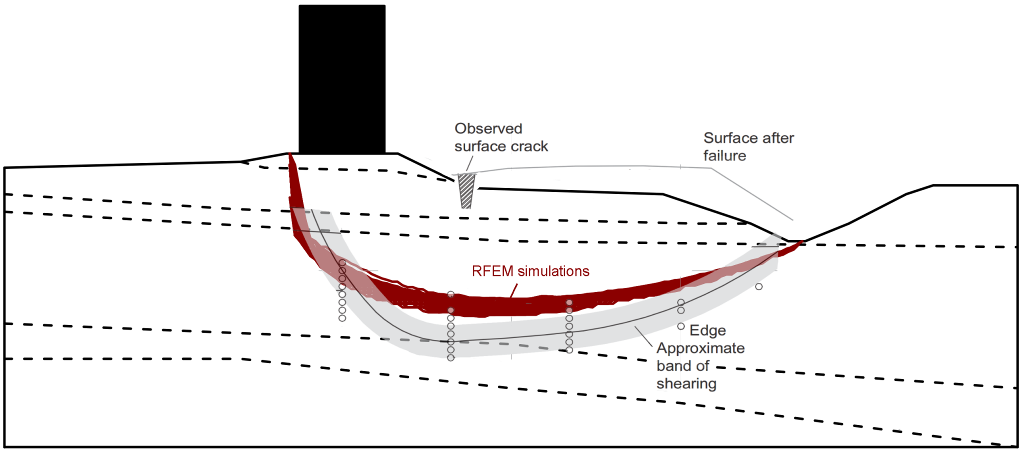

Figure 4.5: Comparing simulated RFEM failure modes to field observations presented in Lehtonen et al. (2015).

4.4 The spatial effect of apparent preconsolidation pressure on failure load

In order to better understand how the variation of preconsolidion pressure effects the stability of Perniö embankment, the simulations with the largest and lowest failure load, F_{max} and F_{min} is compared in Figure 4.6. The figure show: in (a) and (b) the spatial variation of OCR the two cases. Where, (a) corresponds to the case of the lowest failure load and (b) to the highest. By a visually examination, the two cases looks remarkably similar, yet the OCR raster is the only difference affecting the failure load between them. However, some locations are exposed for more stress during loading, note the contours in the image corresponding to the total displacements. The value of apparent preconsolidation pressure are most critical for those cells which exposed for more displacements.

To better compare (a) and (b) the difference between them, $OCR\,F_{max}$ - OCR F_{min}, is shown in (c). Red cells indicates the location of a positive difference, which means lower OCR and shear strength.

Three things becomes evident: firstly, the OCR difference is not uniform, and variate over the area with green and red indicates zones corresponding to areas of higher and lower shear strength. Secondly, the location of the OCR is critical for the embankment stability. Most of the cells show higher strength difference (green), but there is a critical area appearing below the embankment in red, where stresses and strains also are the largest. Thirdly, the critical area is in-between the location of borehole 43 and 44, emphasizing that the spatial location of samples are critical in order to decrease the uncertainty in failure load.

(a) Spatial variation of OCR for maximal stability: $F_{max} = 105\,kPa$

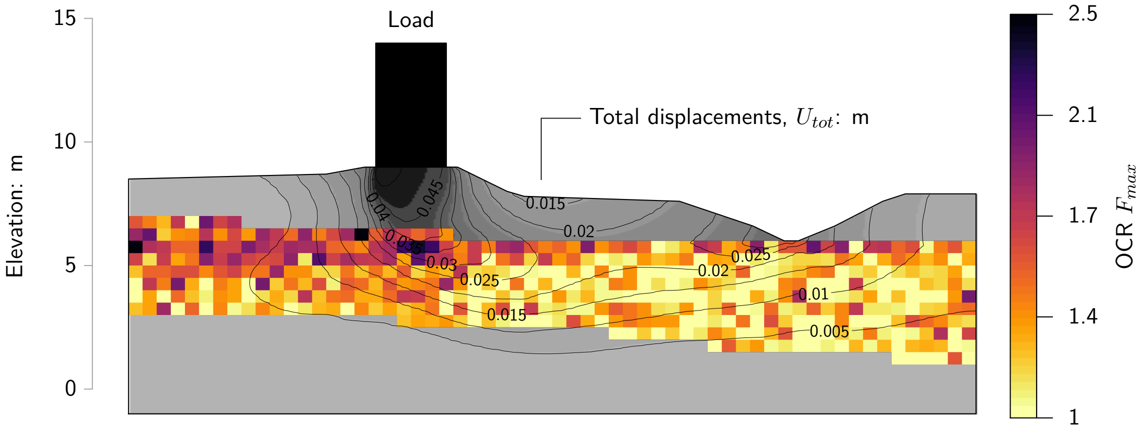

(b) Spatial variation of OCR for for minimal stability: $F_{min} = 70\,kPa$

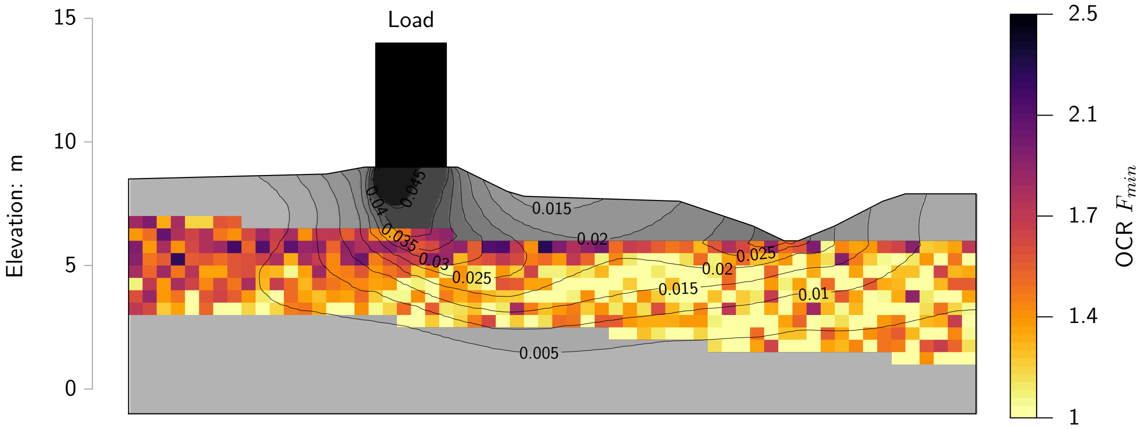

(c) OCR difference:

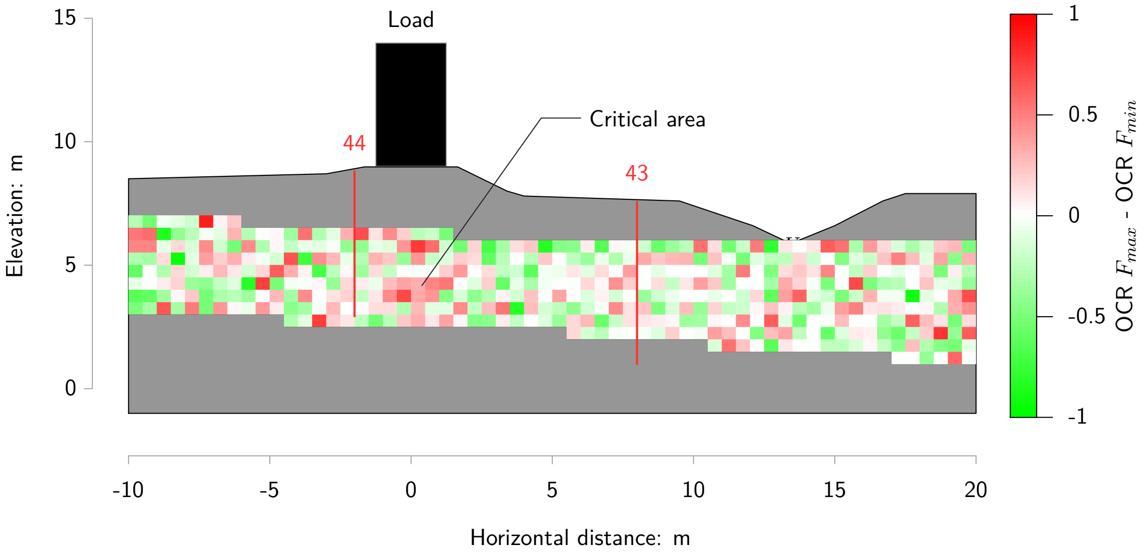

Figure 4.6: The resulting OCR variation for: (a), the largest failure load F_{max}; (b), the smallest failure load F_{min} ; and (c), the OCR difference between (a) and (b).

5 Conclusions & Recommendations

The uncertainties of the inherent variability of preconsolidation pressure on the Perniö test embankment was successfully modelled and compared with previous deterministic investigations and field observations from the failure test. The main findings and recommendations for future research are as follows:

C1 Even with the limitations of: an relative small number of simulations $n = 500$ and coarse raster resolution, the RFEM model shows promising results in estimating the uncertainty of the embankment failure load.

C2 The failure load is highly influenced by the spatial variation of consolidation pressure, ranging approximately 10% from 72 to 107 kPa. This range highlights the limitations of one single deterministic ULS analysis and its justification comparing performance between different soil models by such an approach.

C3 The cumulative distribution function (CDF) of the failure load is not normally distributed. Most failures occur in two groups, perhaps due to bias in raster size. It still is possible, however, to determine the probability of failure and a majority of the failures occur between 82 and 98 kPa. This range is similar to the deterministic max/min analysis. It is unclear if this finding is by chance, site specific or indicating a general rule. If it is the latter, that can justify less computational greedy algorithm in future research, such as for example a point estimate method.

C4 The most critical spatial location, regarding the uncertainty of preconsolidaion pressure on failure load, is found to be below the embankment where the shear stresses and strains are largest. Unfortunately, no samples were taken at this specific location. In case of available measurements from that location, the uncertainties of failure load due to spatial variation of preconsolidaion pressure would have significantly decreased. This emphasizes the importance of not only taking a large numbers of samples, but also the relevance in choosing the sampling location.

C5 Since the test embankment used for validation failed due to creep, the critical horizontal displacement just before failure is hard to determine. It is found that the resulting RFEM pre-failure horizontal displacements ranges from 10 to 40 mm. A large range, but all results are considered realistic compared to observations. This, again, indicates the uncertainties in calculating and trusting a single maximal limit value of horizontal displacements before failure from deterministic analysis.

C6 One single failure mode is found for the embankment. A rotational failure, with a cross-sectional surface area in plane-strain, ranging between 37 to 54 m^2. In the present analysis the failure mode and area is independent of failure load and spatial variation of preconsolidation pressure.

C7 The 17 samples from the two boreholes, are insufficient to evaluate the spatial variation parameters θ and ξ of the site with high accuracy. This leads to an variogram model bias which is not included in this Thesis.

R1 More research is needed in order to estimate the spatial variation parameters of (soft) soil in a more reliable manner, together with the influence on stability due to the number of samples on the Perniö test site.

R2 It would also be of interest to benchmark different constitutive models by a probabilistic approach on the Perniö test site in order to determine the sensitivity of each model for parameter variation.

References

Akbas, B. (2015). Probabilistic Slope Stability Analysis Using Limit Equilibrium, Finite Element and Random Finite Element Methods. Master's thesis, Middle East Technical University.

Alén, C. (1998). *On probability in geotechnics: random calculation models exemplified on slope stabiblity analysis and ground-superstructure interaction.* PhD thesis.

Baecher, G. B. and Christian, J. T. (2003). *Reliability and statistics in geotechnical engineering.* John Wiley & Sons Ltd, The Atrium, South Gate, Chichester, West Sussex, England.

Bakhtiari, S. (2011). *Stochastic Finite Element Slope Stability Analysis.* PhD thesis, University of Manchester.

EN 1997-1:2004 (2004). Eurocode 7: Geotechnical design - part 1: General rules. Standard, European Committee for Standardization (CEN), Brussels.

Fenton, G. A. and Griffiths, D. V. (2008). *Risk assessment in geotechnical engineering.* John Wiley & Sons, Hoboken, New Jersey. USA.

Gras, J. P., Sivasithamparam, N., Karstunen, M., and Dijkstra, J. (2017). Permissible range of model parameters for natural fine-grained materials. *Acta Geotechnica.*

Griffiths, D. V. and Fenton, G. A. (2007). *Probabilistic Methods in Geotechnical Engineering.* Springer, Italy.

GTK (2017). Geological Survey of Finland. `http://en.gtk.fi/informationservices/map_services`. [Online; accessed 19-03-2017].

Hicks, M. A. (2005). Risk and variability in geotechnical engineering. *Géotechnique*, 55(1):1–2.

Hicks, M. A. and Jommi, C. (2014). ALERT Doctoral School 2014 Stochastic Analysis and Inverse Modelling. page 290.

Kobayashi, H., Mark, B. L., and Turin, W. (2012). *Probability, random processes, and statistical analysis.* Cambridge University Press, Cambridge ; New York.

Laaha, G. (2016). 851.311 environmental statistics. Lecture slides.

Larsson, S., Stille, H., and Olsson, L. (2005). On horizontal variability in lime-cement columns. *Géotechnique*, 55(1):33–44.

Lehtonen, V. J., Meehan, C. L., Länsivaara, T. T., and Mansikkamäki, J. N. (2015). Full-scale embankment failure test under simulated train loading. *Géotechnique*, 65(12):961974.

Lethonen, V. (2011). Instrumentation and analysis of railway embankment failure experiment - a general summary. page 52 p.

Mansikkamäki, J. N. (2015). *Effective Stress Finite Element Stability Analysis of an Old Railway Embankment on Soft Clay.* PhD thesis, Tampere University of Technology.

Mataić, I. (2016). *On structure and rate dependence of Perniö clay.* PhD thesis, Aalto University.

Matthews, C., Farook, Z., and Helm, P. (2014). Slope stability analysis -limit equilibrium or the finite element method? *Ground Engineering*, 48(5):22–28.

Olea, R. A. (1991). *Geostatistical Glossary and Multilingual Dictionary.* Oxford University Press, New York.

Pekaje (2017). en.wikipedia.org. `https://en.wikipedia.org/wiki/Accuracy_and_precision#/media/File:Accuracy_and_precision.svg`. Figure created by Anthony Cutler, using en:xfig, en:inkscape, and en:HTML Tidy. Accessed: 2017-06-27.

Peschl, G. M. and Schweiger, H. F. (2003). Reliability Analysis in Geotechnics with Finite Elements—Comparison of Probabilistic, Stochastic and Fuzzy Set Methods. *Isipta*, pages 1–15.

Phoon, K. K. and Retief, J. V. (2016). *Reliability of Geotechnical Structures in ISO2394.* CRC Press, Leiden, The Netherlands.

Ribeiro, P. J. and Diggle, P. J. (2016). geoR: Analysis of Geostatistical Data. *R package version 1.7-5.2*, pages https://CRAN.R–project.org/package=geoR.

Réthāti, L. (1988). *Probabilistic solutions in geotechnics*, volume 46. Elsevier, New York.

Schuppener, B. and Heibaum, M. (2011). In *Proceeding from the 3th International Symposium on Geotechnical Safety and Risk (ISGSR 2011).*

Soulié, M., Montes, P., and Silvestri, V. (1990). Modelling spatial variability of soil parameters. *Canadian Geotechnical Journal*, 27(5):617–630.

Vanmarcke, E. H. (1977). Probabilistic modeling of soil profiles. *Journal of the geotechnical engineering division*, 103(11):1227–1246.

Vanmarcke, E. H. (1984). *Random fields: analysis and synthesis.* MIT Press, Cambridge,MA.

Wackernagel, H. (2003). *Multivariate Geostatistics: An Introduction with Applications, 3rd edition.* Springer-Verlag, Berlin ; Germany.

Appendix A *Perniö test site location*

A.1 Data availability

Measured site dataset accessed from the open databank at: http://urn.fi/urn:nbn:fi:csc-kata20150507094517332534. Soil data from S2010 and S2009 was procvided by (Mataić, 2016).

A.2 Location maps

Perniö is located in south west Finland about 140 km west from Helsinki. The test site is located on an old railway embankment on N 60.26945ř E 023.13171ř (WGS84) marked with red circle on the map in figure A.1.

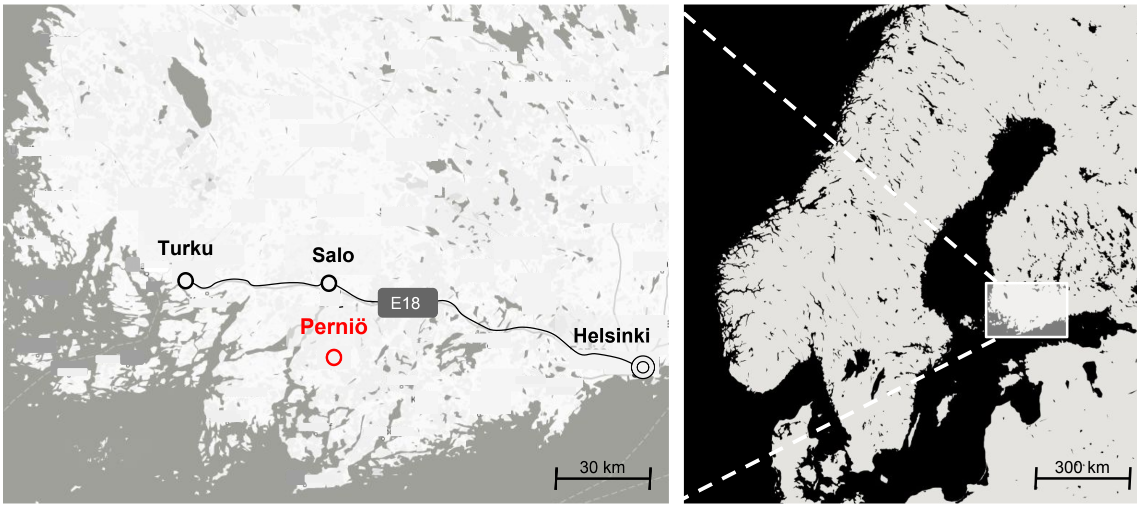

Figure A.1: Geographical location of Perniö testing site.

The test site surrounding is relatively flat, with agriculture lands, ranging from + 4 to + 8 meters above sea level. The test site can be studied on a local scale (1:8000) in Appendix A, which includes three maps: a elevation map, with the geographic location of the site in the center; a aerial map, with hill-shade to indicate the relief and finally a soil map, illustrating the geology of the top soils. All maps were extracted from the Geological Survey of Finlands (GTK) online database (GTK, 2017).

The Lithostratigraphic conditions on site are predominatly soft glacial marine clay of variable thickness on top of moraine and bedrock formations (Lethonen, 2011). The conditions are typical of south Finland, where the Baltic ice lake submerged the lands after the glaciation retreated.

A.3 Elevation map, scale 1:8000

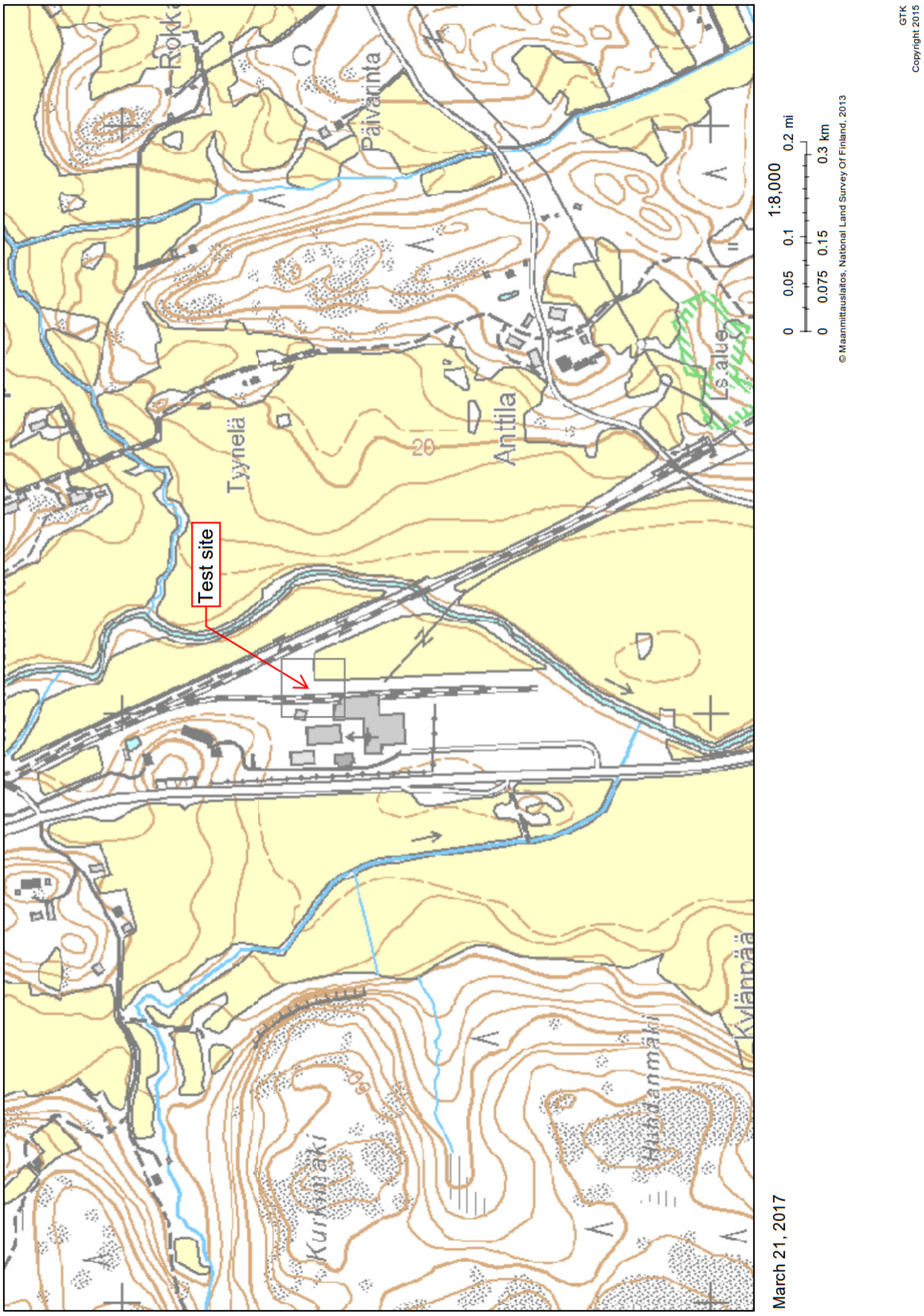

March 21, 2017

© Maanmittauslaitos, National Land Survey Of Finland, 2013

GTK
Copyright 2015

A.4 Aerial map, scale 1:8000

A.5 Soil map, scale 1:8000

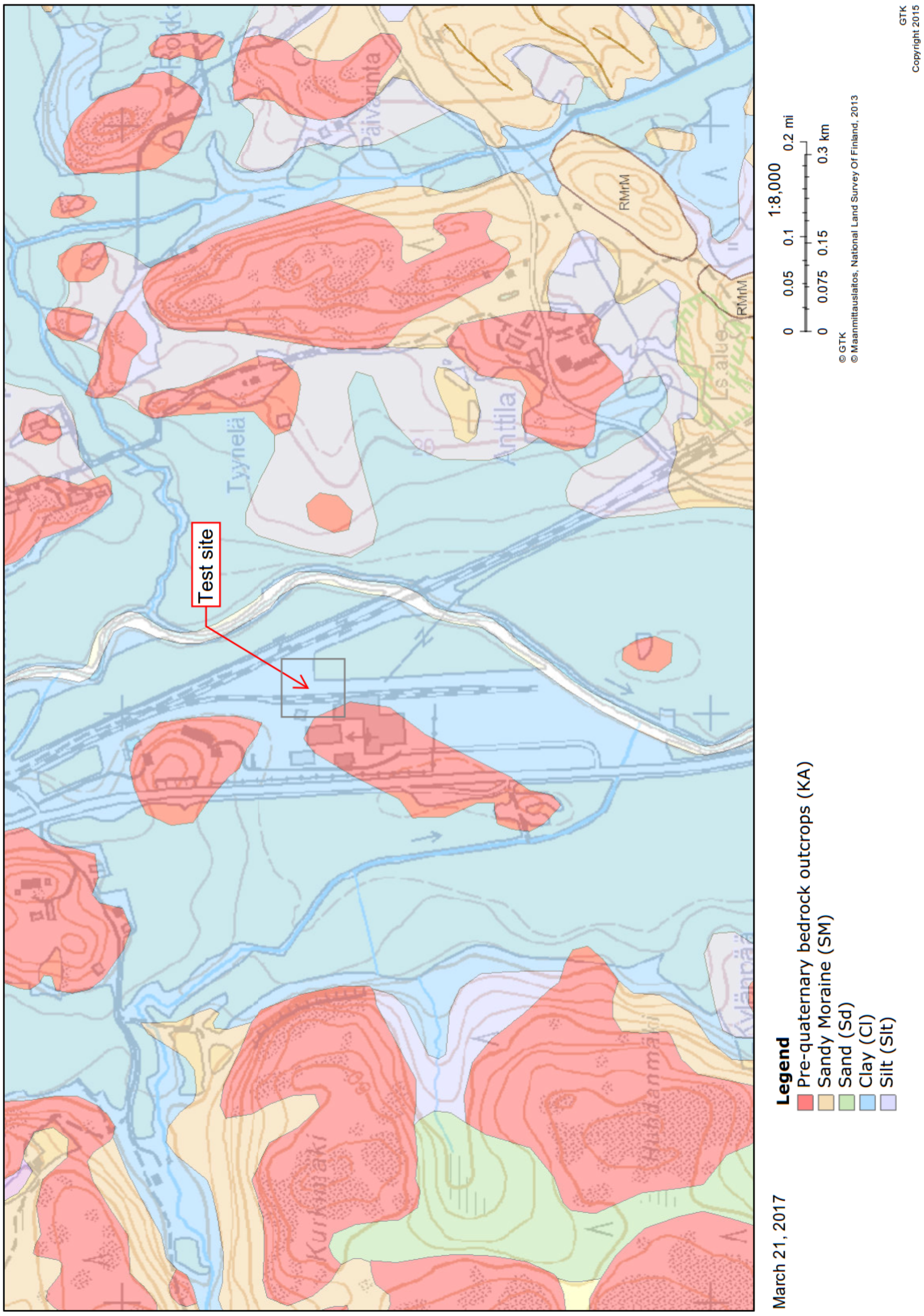

March 21, 2017

© GTK
© Maanmittauslaitos, National Land Survey Of Finland, 2013

GTK
Copyright 2015

Appendix B *Perniö Test data*

B.1 Site investigation Perniö

The site investigation map by Lethonen (2011).

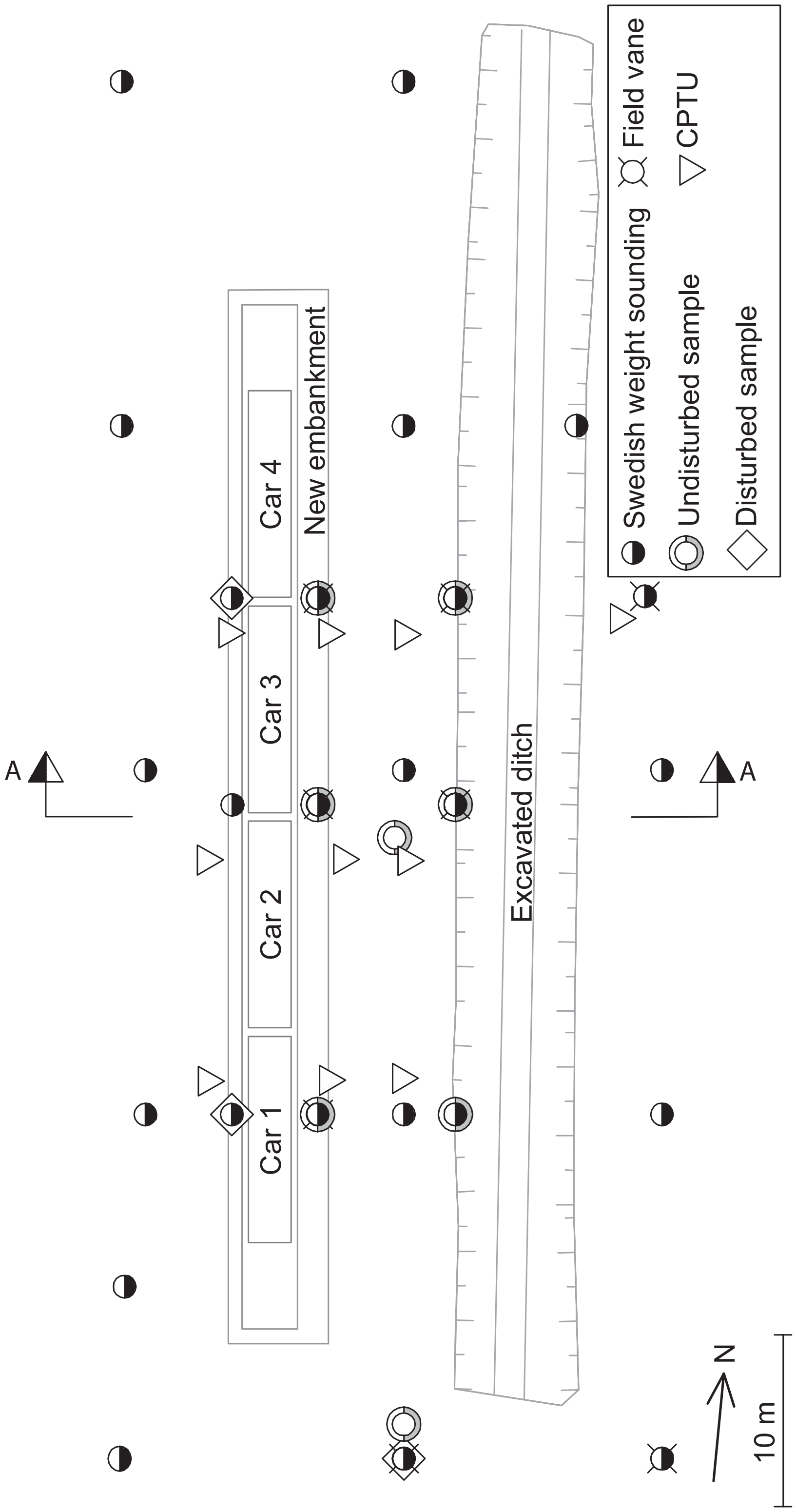

B.2 Instrument locations Perniö

The measuremnt instrumentation map by Lethonen (2011).

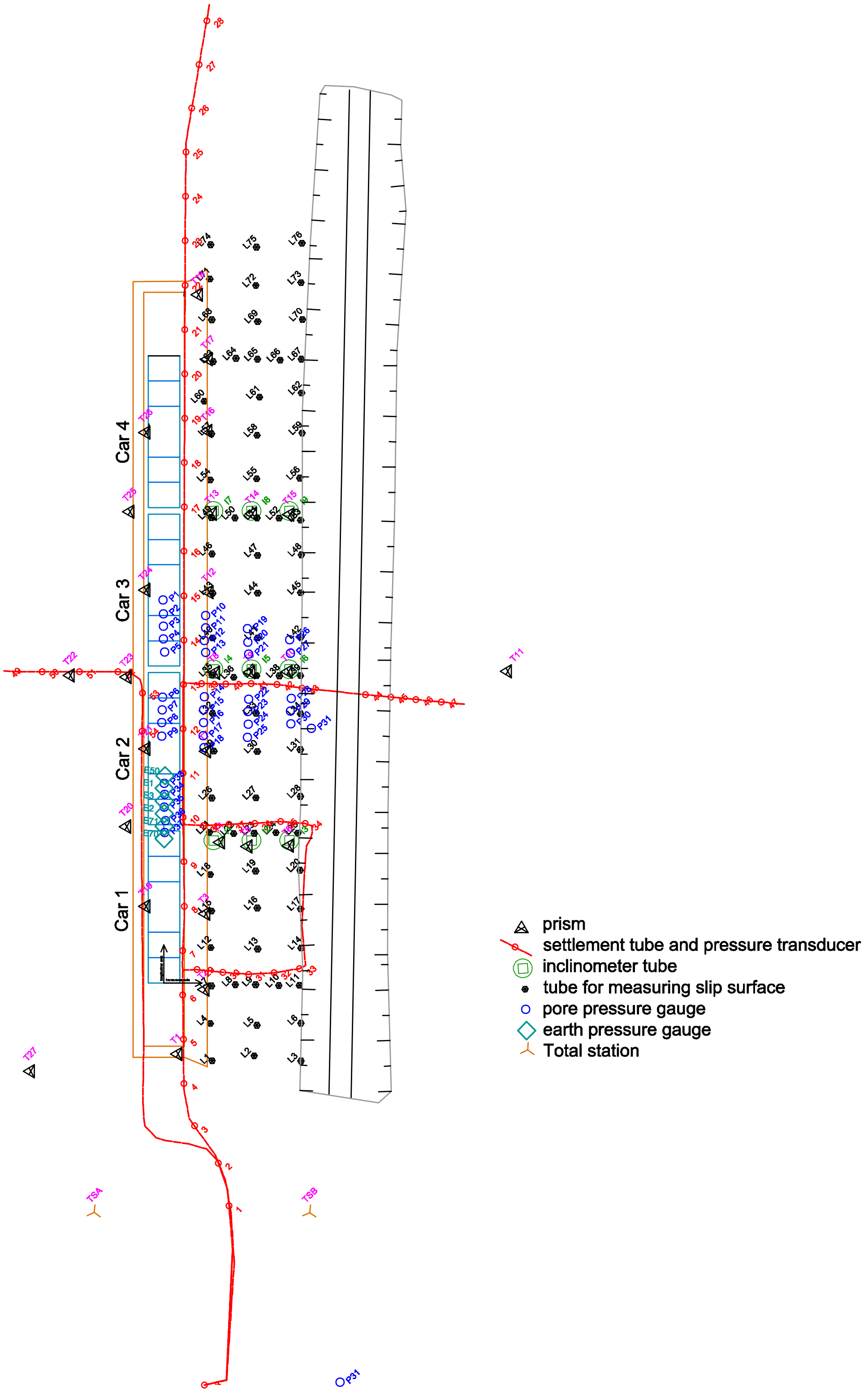

Appendix C

Table C.1: Summary of borehole data used for the study at the Perniö test embankment.

Borehole No 43/45. Sample ID	Borehole	Type	Elevation	x	σ_{pre}	σ'_v	OCR
5666	43	ODE	6,76	-2	35	21,6	1,61
5651	43	ODE	5,71	-2	55	26,8	2,05
5652	43	ODE	4,86	-2	43	31,1	1,38
5653	43	ODE	3,91	-2	48	35,9	1,33
5667	43	ODE	3,01	-2	51	40,3	1,26
5660	45	ODE	4,41	-2	47	33,3	1,40
5662	45	ODE	3,61	-2	46	37,3	1,23
5663	45	ODE	2,71	-2	51	41,8	1,21
Borehole No 44. Sample ID	Borehole	Type	Elevation	x	σ_{pre}	σ'_v	OCR
D57	44	CRS	2,30	8	45	43,9	1,02
5672k	44	ODE	5,56	8	48	27,6	1,73
5669	44	ODE	5,11	8	31	29,8	1,04
5641	44	ODE	5,36	8	30	28,6	1,04
5647	44	ODE	3,98	8	34	35,5	0,95
5668	44	ODE	3,12	8	50	39,8	1,25
5642	44	ODE	3,09	8	60	39,9	1,50
5643	44	ODE	2,24	8	50	44,2	1,13
5648	44	ODE	1,23	8	50	49,2	1,01